

**EFFECTS OF TARGET NUCLEAR EXCITATIONS ON
FUSION REACTIONS**

by

NGOEPE M.M

submitted in accordance with the requirements for
the degree of

MASTERS OF SCIENCE

in the subject

PHYSICS

at the

UNIVERSITY OF SOUTH AFRICA



SUPERVISOR: PROF. M L LEKALA

CO-SUPERVISOR: DR. B. MUKERU

AUGUST 2021

Dedication

To my parents Mr M.E and Mrs M.F Ngoepe for their everlasting support throughout this journey.

When things go wrong as they sometimes will,
When the road you're trudging seems all uphill,
When funds are low and debts are high
And you want to smile , but you have to sigh,
When care is pressing you down a bit,
Rest if you must, but don't you quit.

John Greenleaf Whittier
(1807-1892)

Acknowledgements

First and foremost I would like to give praises to the Lord God for granting me with the opportunity to conduct this research.

∞Special thanks to the following people

- Prof ML Lekala for believing that I had what it takes to become a MSc candidate at UNISA and for opening the doors whenever I came knocking.
- Dr B Mukeru for the everlasting support and guidance he gave me whenever I hit a bump in my research, for the advices shared and introduction to research field.
- Mr J VanRooyen for keeping in touch as my motivator throughout the years

∞The following organisations should also be mentioned

- Armscor for all the financial support they provided
- JINR for giving me the opportunity and exposure during the 2017 student practice
- Members of UNISA physics department for taking their time in reviewing my proposal and dissertation
- Anyone who contributed to my well-being and toward my completion of this degree

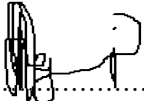
Lastly I would like to thank my family for believing in me and motivating me every time the road travelled got hard.

Declaration

I Mamaropeng Matshidisho Ngoepe declare that the contents of this thesis "**EFFECTS OF TARGET NUCLEAR EXCITATIONS ON FUSION REACTIONS**" is my work and that all the sources quoted have been mentioned and acknowledged by means of complete references.

I further declare that I submitted the dissertation to originality checking software and that it falls within the accepted requirements of originality.

I further declare that I have not previously submitted this work, or part of it, for examination at Unisa for another qualification or at any other higher education institution



.....

20-08-2021
.....

Signature

Date

Ngoepe MM

(student number: 64876306)

Summary

In this work we analyse fusion cross-section (σ_F) in different projectile target systems. Collision systems can result in different reactions such as elastic/ inelastic scattering, fusion and fission reactions to name a few. In this paper, we will be doing a systematic study of light projectile collision, medium projectile collisions and heavy projectile collisions. To this end we should be able to relate fusion cross-section to the size of the projectile. Fusion analysis has played a major role in synthesis of super heavy elements and simulations of supersonic reactions. To understand the fusion analysis, we first take into account the state of no internal excitations of the collision partners (spherical collision). In this case, the target orientation and the radial distance between colliding nuclei are the factors of which σ_F is dependent on. We analyse how the target orientation affects the Coulomb potential which significantly gives us the effect on fusion.

Secondly, we look at the case of deformed target nucleus. The target deformations considered in this paper include rotational deformation, vibrational deformations and neutron transfer reactions. The full-coupled channel program (CCFULL) is used to couple the rotational excitations to the radial part. With this program, we are able to analyse how each deformation parameter affects fusion cross-section. We can also make sense of fusion at energies below and around the Coulomb barrier. The barrier distribution calculations gives us a great insight of how each deformation parameter lowers the barrier and at which energy regions. For vibrational coupling calculations, the cross-section can be compared to that of rotational coupling and spherical collisions in order to see which parameters enhance fusion the most and at which energies. In the case of neutron transfer reactions, we analyse how the Q-value relates to fusion enhancement. For each system where neutron transfer was considered, we look at the possibility and comparison of +1neutron, +2neutrons and +3neutrons transfer channels. We further look into details how the fusion barrier distribution data relates to the cross-sections.

For quantitative analysis in this work, the systems investigated were:

- ${}^6,7\text{Li}$ projectiles with ${}^{28}\text{Si}$, ${}^{64}\text{Zn}$, ${}^{152}\text{Sm}$, ${}^{198}\text{Pt}$ & ${}^{209}\text{Bi}$ targets
- ${}^{40}\text{Ca}$ projectile with ${}^{62,64}\text{Ni}$, ${}^{96}\text{Zr}$, ${}^{194}\text{Pt}$ & ${}^{238}\text{U}$ targets

KEY WORDS

- Fusion
- Spherical collision
- Deformations
- Coulomb barrier
- Barrier position
- Rotational coupling
- Neutron transfer
- Barrier distribution
- Nuclear parameters
- Total potential

Contents

1	INTRODUCTION	1
2	Coupled channels formalism for fusion reactions	4
2.1	Coupled Channels equations	4
3	Fusion cross sections of $^{6,7}\text{Li}$-induced reactions	10
3.1	Case of spherical projectile and target nuclei	10
3.1.1	Description of fusion potentials	10
3.1.2	Convergence of fusion cross sections	12
3.1.3	Comparison with the experimental data	15
3.2	Case of a deformed target	16
4	Fusion cross sections of ^{40}Ca-induced reactions	21
4.1	Case of spherical projectile and target nuclei	22
4.1.1	Convergence analysis	22
4.1.2	Comparison with experimental data	24
4.2	Deformation of the target nucleus	25
4.3	Effects of vibration	29
4.4	Multi-neutron transfer effects	30
4.5	Fusion barrier distribution	32
5	Conclusions	38
	References	41

List of Tables

3.1	Parameters V_0 , r_0 , and a_0 of the Wood-Saxon potential, for the different reactions considered. The reduced radii r_0 are converted to absolute ones as The nuclear radius is given by $R_0 = r_0(A_p^{1/3} + A_t^{1/3})$	11
3.2	Potential deformation parameters of target nuclei under investigation obtained from Ref.[3].	17
4.1	Parameters V_0 , r_0 , and a_0 of the ^{40}Ca -target nuclear potentials. The absolute radii are obtained from the reduced one (r_0) as $R_0 = r_0(A_p^{1/3} + A_t^{1/3})$	22
4.2	Values of the maximum integration parameter (r_{max}), wavenumber (k), and maximum angular momentum (ℓ_{max}), obtained from Eq.(4.1), for the different targets considered. The wave-number was calculated at $E_{\text{c.m.}} = V_B$	23
4.3	Deformation parameters and associated energies for $^{62,64}\text{Ni}$, ^{96}Zr , ^{194}Pt and ^{238}U obtained from Ref [3].	26
4.4	Deformation parameters used in vibrational coupling for $^{62,64}\text{Ni}$, ^{96}Zr , ^{194}Pt and ^{238}U targets.	29
4.5	Q-values (MeV) for neutron transfer in various heavy ion systems of ^{40}Ca projectiles.	31
4.6	Fusion barrier distribution peak positions displayed in Fig.4.9. V_B is the nominal barrier shown by the downwards arrow in Fig.4.8. V_{TD}^L and V_{TD}^H are peak positions in Fig.4.9 for low and high V_0 respectively	36

List of Figures

3.1	Plots of nuclear, $V_N(r)$, Coulomb $V_C(r)$, and total potentials $V(r)$, as functions of the radial distance (r), for different interacting systems.	12
3.2	Convergence of the fusion cross sections as functions of the center-of-mass incident energy($E_{c.m}$), with respect to the numerical integration r_{max} , for ${}^6,7\text{Li}$ projectiles	14
3.3	Comparison of the theoretical calculations with experimental data for ${}^6\text{Li}$ projectile. The data were obtained from [41], for ${}^{28}\text{Si}$, [35], for ${}^{64}\text{Zn}$, [31], for ${}^{152}\text{Sm}$, [40], for ${}^{198}\text{Pt}$ and [38], for ${}^{209}\text{Bi}$ target nuclei. The data were obtained from [36], for ${}^{28}\text{Si}$, [35], for ${}^{64}\text{Zn}$, [30], for ${}^{152}\text{Sm}$, [34], for ${}^{198}\text{Pt}$ and [33], for ${}^{209}\text{Bi}$ target nuclei.	16
3.4	Plots of deformed total potential for different interacting systems. "Sph" represent a spherical target, i.e, when no deformations are included, "T Def" stands for target deformation, when both β_2 and β_4 are included simultaneously.	18
3.5	Fusion cross sections of ${}^6,7\text{Li}$ projectiles on different target masses. For ${}^6\text{Li}$ projectile, experimental data were taken from [41] (${}^{28}\text{Si}$), [35] (${}^{64}\text{Zn}$), ${}^{152}\text{Sm}$ [31], ${}^{198}\text{Pt}$ [40] and ${}^{209}\text{Bi}$ [38]. For ${}^7\text{Li}$ projectile, they were taken from ${}^{28}\text{Si}$ [36], ${}^{64}\text{Zn}$ [35], ${}^{152}\text{Sm}$ [30], ${}^{198}\text{Pt}$ [34] and ${}^{209}\text{Bi}$ [33].	20
4.1	Effect of angular momentum ℓ on the Coulomb pocket.	23
4.2	r_{max} convergence for heavy-heavy fusion reaction.	24
4.3	Comparison of the fusion experimental data with the one-dimensional potential model, in reactions induced by ${}^{40}\text{Ca}$ projectile. The experimental data taken from Ref.[18] for ${}^{62}\text{Ni}$, [20] for ${}^{64}\text{Ni}$, [21] for ${}^{96}\text{Zr}$, [22] for ${}^{194}\text{Pt}$ and [24] for ${}^{238}\text{U}$	25

4.4	Deformed total potential for heavy-heavy collision systems. 'Sph' corresponds to spherical target where no deformations are included. The label 'T Def' is the deformed target where both β_2 and β_4 have been included and the labels β_2 and β_4 corresponds to calculations where only β_2/β_4 deformations are included.	27
4.5	Fusion cross sections in reactions induced by ^{40}Ca projectile, obtained when target deformations are included in the calculations. The experimental data taken Ref. [18] for ^{62}Ni , [20] for ^{64}Ni , [21] for ^{96}Zr , [22] for ^{194}Pt and [24] for ^{238}U	28
4.6	Effects of target vibration on fusion compared to rotational deformation and inert data.	30
4.7	Effects of +1n, +2n and +3n transfer channels on fusion cross sections. The experimental data for ^{62}Ni , ^{64}Ni , ^{96}Zr , ^{194}Pt and ^{238}U are obtained from Refs. [18, 20, 21, 22, 24] respectively.	32
4.8	Effect of target β_2 and β_4 deformations on the fusion barrier distributions for ^{40}Ca -induced reactions. Label "Sph" represents the data for spherical collision where the deformation parameters are set to zero. "T Def" represents the data where both β_2 and β_4 parameters are considered.	34
4.9	Comparison of fusion barrier distribution data for V_0 given in Table.4.1 and V_0 given in Fig.4.5 that agrees with the experimental data.	35
4.10	Effect of +1n,+2n and +3n transfer channel on fusion barrier distributions for ^{40}Ca -induced reactions. Label "Sph" represents the data for spherical collision where there is no target excitations.	37

Chapter 1

INTRODUCTION

The study of nuclear reactions, such as elastic scattering, fusion, breakup, among others, have gained extensive attention over the past few decades (see for example Refs.[5, 6, 9, 10, 11, 15, 23, 32, 37, 38, 42, 56] for some of the recent review on these subjects). Although the study of fusion reactions can be traced over a century back, a full understanding of reaction dynamics that lead to fusion enhancement or suppression is far from being settled. One of the reasons is the many number of degrees of freedom involved during nuclear reactions.

Nuclei are not inert entities, that is their internal structure would play a important role in the fusion process. This is due to the possible rotational and /or vibrational states of the nuclei caused by their intrinsic motion. Historically the crucial role of the nuclear internal structure came to light when the simple theoretical one-dimensional potential model failed to describe fusion cross section experimental data for incident energies above the Coulomb barrier (see for example Ref. [15]). For incident energies well above the Coulomb barrier, this model provides a better fit of the experimental data,for a wide range of fusion reactions. In this model, the interacting particles are assumed to be inert, i.e., without internal structure, such that their relative motion is only described by the relative coordinate between their centre-of-mass. Therefore, the failure of this model to describe the data emphasizes its flaw at these energies (for incident energies below and around the Coulomb barrier). On the other hand, its successful description of the data above the Coulomb barrier emphasizes the irrelevance of the nuclear internal structure in

this energy region. This shows clearly that fusion dynamics below and above the Coulomb barrier are fundamentally different. One of these differences is due to a stronger Coulomb repulsion below the Coulomb barrier, such that for fusion to occur, the fusing particles must tunnel through the barrier. It follows that any reaction mechanism that lowers the Coulomb barrier, will definitely serve to enhance the fusion cross section.

It is well known that nuclear internal degrees of freedom, such as nuclear excitations, deformations, among others, play an important role in the analysis of the experimental data below the Coulomb barrier, as exemplified by Ref.[1, 2, 8, 15, 25, 26, 28, 29, 39, 63]. Therefore, a successful modelling of fusion reactions below the barrier, needs to consider not only the relative centre-of-mass motion of the interacting particles, but also their internal motions and deformations. The internal states are eigenfunctions of the internal Hamiltonian, and hence are obtained by diagonalizing the Hamiltonian through a solution of the corresponding Schrödinger equation. The projectile and target internal states form a complete basis on which the projectile-target wave function is expanded.

On the practical side, the substitution of this expansion into the system Schrödinger equation, yields a set of coupled differential equations. The number of such coupled equations to be solved can quickly grow to outperform nowadays computer capacities, depending on the number of internal states that need to be included. For numerical purpose, these equations are truncated to a finite number through different theoretical assumptions, to ensure their numerical tractability.

Neutron transfer channels as well as nuclear deformation parameters such as quadrupole β_2 and hexadecapole β_4 parameters, play an important role in the enhancement of fusion at energies below the Coulomb barrier. These parameters define the intrinsic coordinates of the nucleus and they have been reported to significantly affect fusion cross sections [21, 24, 27, 42, 55, 57, 60, 63, 67, 70, 71, 75, 76]. For instance in Ref.[27, 55, 62], it was found that the β_2 deformation parameter enhances the fusion cross section at lower incident energies, in fusion reactions involving $^{40,48}\text{Ca}$ projectiles. The effects of β_2 deformation was combined with the hexadecapole β_4 deformation to clarify the importance of the

latter on fusion cross section. By analysing fusion barrier distributions of the $^{28}\text{Si} + ^{92}\text{Zr}$ reaction [63], the authors concluded that the fusion process is sensitive to β_4 deformation parameter.

It has been shown that a positive Q -value and multi-neutron transfer influence the transfer channel and enhance fusion cross section at near and below-barrier energies as shown in Refs.[19, 20, 21, 42, 65, 66, 67, 70, 71, 69, 77]. Nuclei with excess neutrons would be expected to induce higher fusion probabilities due to neutron transfer. However, in some cases, the neutron excess itself does not lead to fusion enhancement [67]. This result deserves further investigation, in order to better elucidate under which circumstances this occurs other than a negative Q -value. This would also serve to address the following question. How does the neutron transfer depend on the structure of target nuclei?

In this dissertation, we perform a systematic study of fusion cross sections in reactions involving light and heavy nuclei. The main objectives are: (i) to investigate the interplay of the quadrupole β_2 and hexadecapole β_4 target deformation parameters. Here we aim to study in more detail how the effect of these parameters changes with the projectile and target masses; (ii) to investigate the role multi-neutron transfer channels. To this end, we will separately analyse one-neutron, two-neutron and three-neutron transfer channels. The results are mostly focused on the rotational coupling calculations and will feature some cases where vibrational coupling is considered.

Chapter 2

Coupled channels formalism for fusion reactions

2.1 Coupled Channels equations

When two nuclei interact, many phenomena can take place. For examples, nuclear elastic and inelastic scattering, fission reaction and fusion. In other instances after interaction, the two nuclei can emerge in the exit channel unchanged, in which case the entrance channel is the same as the exit one. This is what happens in the elastic scattering. Another possibility is that after interaction, the two nuclei may excite, and exchange particles. In this work, we are particularly interested in fusion reactions, where the interacting nuclei fuse to form one compound nucleus. For the sake of simplicity, we only present a theoretical description of the case when only the target nucleus is excited. The relative motion of the two interacting nuclei is described by the Schrödinger equation of the form

$$[H(\mathbf{r}, \xi) - E]\psi_J^M(\mathbf{r}, \xi) = 0, \quad (2.1)$$

where E , is the total energy (the projectile incident energy), and $\psi_J^M(\mathbf{r}, \xi)$, the wave function. (Here J is the total angular momentum given by $\mathbf{J} = \boldsymbol{\ell} + \mathbf{I}$, where, $\boldsymbol{\ell}$ is the angular orbital momentum . \mathbf{I} is the target spin and M is the z -projection of J).

ξ represents the target intrinsic coordinates and \mathbf{r} is the radial coordinates for the relative motion of fusing nuclei. The total Hamiltonian $H(\mathbf{r}, \xi)$ shows the coupling between

projectile-target relative motion and the internal structure of the nuclei and is defined as

$$H(\mathbf{r}, \xi) = -\frac{\hbar^2}{2\mu} \nabla^2 + V(r) + H_0(\xi) + V_{\text{cp}}(\mathbf{r}, \xi), \quad (2.2)$$

where $\mu = m_p m_t / (m_p + m_t)$ is the projectile-target reduced mass, with m_p and m_t the projectile and target atomic masses, respectively. ∇^2 is the usual nabla operator. $V(r)$ is the interacting potential consisting of both Coulomb and nuclear components. $V_{\text{cp}}(\mathbf{r}, \xi)$ is the coupling potential that couples different states of the excited nucleus. $H_0(\xi)$ is the internal Hamiltonian whose eigenstates $\phi_{\alpha I m_I}(\xi)$ are the internal states that satisfy the Schrödinger equation

$$H_0(\xi) \phi_{\alpha I m_I}(\xi) = \varepsilon_{\alpha I} \phi_{\alpha I m_I}(\xi), \quad (2.3)$$

where $\varepsilon_{\alpha I}$ are excitation energies, with α a set of relevant quantum numbers that describe an internal state, m_I , the z -projection the spin I . Once the internal states are constructed, the wave function in Eq.(2.1) is obtained as follows:

$$\psi_J^M(\mathbf{r}, \xi) = \sum_{\ell, I} \frac{u_{\ell I}^J(r)}{r} \sum_{m_\ell, m_I} \langle \ell m_\ell I m_I | J M \rangle Y_\ell^{m_\ell}(\hat{\mathbf{r}}) \phi_{\alpha I m_I}(\xi), \quad (2.4)$$

where $u_{\ell I}^J(r)$, is the radial part of the wave function, $\langle \ell m_\ell I m_I | J M \rangle$ are the Clebsh-Gordon coefficients [59], $Y_\ell^{m_\ell}(\hat{\mathbf{r}})$, the usual spherical harmonics associated with the coordinate \mathbf{r} , with m_ℓ the z -projection of ℓ , and $\hat{\mathbf{r}}$ is the solid angle in the direction of \mathbf{r} .

The substitution of expansion (2.4) into the Schrödinger equation (2.1) yields the following set of coupled differential equations

$$\left[-\frac{\hbar^2}{2\mu} \frac{d^2}{dr^2} + \frac{\ell(\ell+1)\hbar^2}{2\mu r^2} + V(r) - E + \varepsilon_{\alpha I} \right] u_\gamma^J(r) = \sum_{\gamma \neq \gamma'} V_{\gamma\gamma'}^J(r) u_{\gamma'}^J(r), \quad (2.5)$$

where $V_{\gamma\gamma'}(r)$, are the coupling matrix elements, that couple different internal states through the coupling potential V_{cp} , with $\gamma \equiv (\alpha, \ell, I)$ a set of relevant quantum numbers, describing a channel, and it is given by

$$V_{\gamma\gamma'}^J(r) = \langle \mathcal{Y}_\gamma(\hat{\mathbf{r}}, \xi) | V_{\text{cp}}(\mathbf{r}, \xi) | \mathcal{Y}_{\gamma'}(\mathbf{r}, \xi) \rangle, \quad (2.6)$$

where the channel wave function $\mathcal{Y}_\gamma(\hat{\mathbf{r}}, \xi)$, is defined as

$$\mathcal{Y}_\gamma(\mathbf{r}, \xi) = \sum_{m_\ell, m_I} \langle \ell m_\ell I m_I | J M \rangle Y_\ell^{m_\ell}(\hat{\mathbf{r}}) \phi_{\alpha I m_I}(\xi). \quad (2.7)$$

To evaluate the coupling matrix elements, we start with the expansion of the coupling potential i.e

$$V_{cp}(\mathbf{r}, \xi) = \sum_{\lambda=0}^{\infty} f_{\lambda}(r) Y_{\ell}^{m_{\ell}}(\hat{\mathbf{r}}) \cdot T_{\lambda}(\xi) \quad (2.8)$$

where $f_{\lambda}(r)$ are potential form factors, and $T_{\lambda}(\xi)$ are the spherical tensors constructed from the intrinsic coordinates. Using the Wigner-Eckart theorem [2, 58] and substituting Eq.(2.7), into Eq.(2.6), the coupling matrix elements reduce to

$$\begin{aligned} V_{\gamma\gamma'}^J(r) &= \sum_{\lambda} (-)^{I-I'+\ell'+J} f_{\lambda}(r) \langle \ell || Y_{\ell}^{m_{\ell}} || \ell' \rangle \langle \alpha I || T_{\lambda} || \alpha' I' \rangle \\ &\times \sqrt{(2\ell+1)(2I+1)} \begin{Bmatrix} I' & \ell' & J \\ \ell & I & \lambda \end{Bmatrix}, \end{aligned} \quad (2.9)$$

where $\{ \dots \}$ are Racah coefficients [58], $\langle \dots || \dots \rangle$, are reduced matrices, with

$$\langle \ell || Y_{\ell} || \ell' \rangle = \sqrt{\frac{(2\ell+1)(2\lambda+1)(2\ell'+1)}{4\pi}} \begin{pmatrix} \ell & \lambda & \ell' \\ 0 & 0 & 0 \end{pmatrix}, \quad (2.10)$$

where (\dots) , are $3j$ coefficients. When the target nucleus is deformed, the radius R_0 is transformed to $R_0 \rightarrow R_0 + \hat{O}$, where R_0 represents the spherical part. The \hat{O} is the coupling Hamiltonian operator for rotational and vibrational couplings given by

$$\hat{O}_{rot} = \beta_2 R_T Y_2(\theta) + \beta_4 R_T Y_4(\theta) \quad (2.11)$$

$$\hat{O}_{vib} = \frac{\beta_{\lambda}}{\sqrt{4\pi}} R_T (a_{\lambda 0}^{\dagger} + a_{\lambda 0}), \quad (2.12)$$

respectively. θ is the orientation angle and β_{λ} are deformation parameters of multi polarity λ . $a_{\lambda 0}^{\dagger}$ and $a_{\lambda 0}$ are phonon creators and annihilators respectively. Therefore, for the rotational couplings, the nuclear matrix elements of the operator \hat{O}_{rot} between states $\langle \gamma | = \langle I0 |$ and $|\gamma' \rangle = |I'0 \rangle$ are given by

$$\begin{aligned} \hat{O}_{rot}(\gamma, \gamma') &= \langle I0 | O_{rot} | I'0 \rangle \\ &= R_T [\beta_2 \langle I0 | Y_2 | I'0 \rangle + \beta_4 \langle I0 | Y_4 | I'0 \rangle] \\ &= \sqrt{\frac{5(2I+1)(2I'+1)}{4\pi}} \beta_2 R_T \begin{pmatrix} I & 2 & I' \\ 0 & 0 & 0 \end{pmatrix}^2 \\ &+ \sqrt{\frac{5(2I+1)(2I'+1)}{4\pi}} \beta_4 R_T \begin{pmatrix} I & 4 & I' \\ 0 & 0 & 0 \end{pmatrix}^2 \end{aligned} \quad (2.13)$$

On the other hand the nuclear matrix elements for the vibrational coupling between the γ and γ' -phonon states $\langle\gamma|$ and $|\gamma'\rangle$, are given by

$$\hat{O}_{\text{vib}}(\gamma, \gamma') = \frac{\beta_\lambda}{\sqrt{4\pi}} R_T \left(\sqrt{\gamma'} \delta_{\gamma, \gamma'-1} + \sqrt{\gamma} \delta_{\gamma, \gamma'+1} \right). \quad (2.14)$$

For the Coulomb interaction, the rotational and vibrational operators are given by

$$\hat{O}_{\text{rot}} = Z_P Z_T e^2 \left[\frac{3R_T^2}{7r^3} \beta_2 Y_2(\theta) + \frac{3R_T^4}{11r^5} \beta_4 Y_4(\theta) \right] \quad (2.15)$$

$$\hat{O}_{\text{vib}} = \frac{\beta_\lambda}{\sqrt{4\pi}} \frac{3}{2\lambda + 3} \frac{R_T^\lambda}{r^{\lambda+1}} Z_P Z_T e^2 \quad (2.16)$$

and the corresponding matrix elements are defined as

$$\begin{aligned} \hat{O}_{\text{rot}}(\gamma, \gamma') &= \frac{3Z_P Z_T e^2 R_T^2}{7} \frac{\beta_2}{r^3} \sqrt{\frac{5(2I+1)(2I'+1)}{4\pi}} \begin{pmatrix} I & 2 & I' \\ 0 & 0 & 0 \end{pmatrix}^2 \\ &+ \frac{3Z_P Z_T e^2 R_T^4}{11} \frac{\beta_4}{r^5} \sqrt{\frac{9(2I+1)(2I'+1)}{4\pi}} \begin{pmatrix} I & 4 & I' \\ 0 & 0 & 0 \end{pmatrix}^2, \end{aligned} \quad (2.17)$$

and

$$\hat{O}_{\text{vib}}(\gamma, \gamma') = \frac{\beta_\lambda}{\sqrt{4\pi}} Z_P Z_T e^2 \frac{3}{2\lambda + 3} \frac{R_T^\lambda}{r^{\lambda+1}} \left(\sqrt{\gamma'} \delta_{\gamma, \gamma'-1} + \sqrt{\gamma} \delta_{\gamma, \gamma'+1} \right). \quad (2.18)$$

The nuclear and Coulomb coupling matrix elements can be obtained from the operator \hat{O} . The nuclear coupling matrix elements are given by

$$V_{\gamma\gamma'}^{(N)}(\mathbf{r}, \hat{O}) = \langle\gamma|V_N(\mathbf{r}, \hat{O})|\gamma'\rangle - V_N(\mathbf{r})\delta_{\gamma\gamma'}, \quad (2.19)$$

where the nuclear coupling potential $V_N(\mathbf{r}, \hat{O})$ is given by

$$V_N(\mathbf{r}, \hat{O}) = \frac{-V_0}{1 + \exp[(r - R_0 - \hat{O})/a]} \quad (2.20)$$

with V_0 and a given *posteriori* by Eqs. (2.26) and (2.27) respectively. The vibration of the target nucleus deforms the potential interactions between the colliding nuclei. The nuclear interaction is assumed to be a function of the separation distance between the projectile and target surfaces, and it is given by

$$V^{(N)}(\mathbf{r}, \alpha_{\ell\mu}) = V_N(\mathbf{r}) - R_T \frac{dV_N(\mathbf{r})}{dr} \sum_{\ell\mu} \alpha_{\ell\mu} Y_\ell^{m_\ell}(\hat{\mathbf{r}}), \quad (2.21)$$

where $\alpha_{\ell\mu}$ is the surface coordinates of the vibrating target nucleus. The Coulomb potential between spherical projectile and the vibrating target is given by

$$V_C(\mathbf{r}) = \int d\mathbf{r}' \frac{Z_T Z_P e^2}{|\mathbf{r} - \mathbf{r}'|} \rho_T(\mathbf{r}'), \quad (2.22)$$

where ρ_T is the charge density of the target nucleus.

In Ref [55], the incoming wave boundary conditions (IWBC) are used to solve the coupled equations. According to IWBC, the incoming waves are recorded at $r = r_{\text{abs}}$, the absorption radius and the outgoing waves are at $r \rightarrow \infty$ for all channels except the entry channel. The following equations show the boundary conditions for when $r \leq r_{\text{abs}}$ and for $r \rightarrow \infty$ where the conditions are defined by the radial part $u_\gamma^J(\mathbf{r})$

$$\begin{aligned} u_\gamma^J(\mathbf{r}) &\sim \sqrt{\frac{k_\gamma}{k_{\gamma'}(r)}} \mathcal{T}_{\gamma\gamma'}^J \exp\left(-i \int_{r_{\text{abs}}}^r k_\gamma(r') dr'\right), & r \leq r_{\text{abs}} \\ &\rightarrow H_{\ell_\gamma}^{(-)}(k_\gamma r) \delta_{\gamma\gamma'} - \sqrt{\frac{k_\gamma}{k_{\gamma'}}} \mathcal{S}_{\gamma\gamma'}^J H_{\ell_\gamma}^{(+)}(k_\gamma r), & r \rightarrow \infty \end{aligned} \quad (2.23)$$

where $H_{\ell_\gamma}^{(-)}(k_\gamma r)$ and $H_{\ell_\gamma}^{(+)}(k_\gamma r)$ are the incoming and outgoing Coulomb Hankel functions respectively. γ describes the set of quantum numbers at the entry channel and γ' the exit channel. r_{abs} is the absorption radius and $\mathcal{T}_{\gamma\gamma'}^J$ are the transmission coefficients. $\mathcal{S}_{\gamma\gamma'}$ is the scattering S matrix[15]. $k_\gamma(\mathbf{r})$ is the local wave number for channel γ and it is given by

$$k_\gamma(\mathbf{r}) = \sqrt{\frac{2\mu}{\hbar^2} \left(E - \varepsilon_\gamma - \frac{\ell_\gamma(\ell_\gamma + 1)\hbar^2}{2\mu r^2} - V_N(\mathbf{r}) - V_C(\mathbf{r}) - V_{\gamma\gamma'}(\mathbf{r}) \right)} \quad (2.24)$$

where $V_C(\mathbf{r}) = \frac{Z_T Z_P e^2}{r}$ is the Coulomb potential and $V_N(\mathbf{r})$ is the bare nuclear potential defined by the Wood-Saxon model as

$$V_N(\mathbf{r}) = \frac{-V_0}{1 + \exp[(r - R_0)/a]}, \quad (2.25)$$

with $R_0 = R_P + R_T$, for $R_x = r_0 A_x^{(1/3)} \text{fm}$ ($x = P, T$). V_0 the potential depth given by

$$V_0 = 16\pi\eta\mu \times a, \quad (2.26)$$

where μ is the projectile-target reduced mass. η is defined as

$$\eta = 0.95 \left[1 - 1.81 \left(\frac{N_P - Z_P}{A_P} \right) \left(\frac{N_T - Z_T}{A_T} \right) \right] \text{MeV/fm}^2$$

and a is the surface diffuseness parameter given by

$$a = \left[\frac{1}{1.17 \left[1 + 0.53 \left(A_P^{-1/3} + A_T^{-1/3} \right) \right]} \right] \text{fm}. \quad (2.27)$$

At $r = r_{\text{max}}$, the obtained wave function of the γ' channel $\mathcal{X}_{\gamma\gamma'}(\mathbf{r})$ is given by

$$\mathcal{X}_{\gamma\gamma'}(\mathbf{r}) = A_{\gamma\gamma'} H_{\ell_\gamma}^{(-)}(k_\gamma r_{\text{max}}) + B_{\gamma\gamma'} H_{\ell_\gamma}^{(+)}(k_\gamma r_{\text{max}}), \quad (2.28)$$

where the coefficients $A_{\gamma\gamma'}$ and $B_{\gamma\gamma'}$ are obtained by matching the ratio of wave function at $r_{\max} - h$ and $r_{\max} + h$. The coupled channel equation is then given by linear combination of $\mathcal{X}_{\gamma\gamma'}(\mathbf{r})$ as

$$\Psi_{\gamma'}(\mathbf{r}) = \sum_{\gamma} \mathcal{T}_{\gamma\gamma'} \mathcal{X}_{\gamma\gamma'}(\mathbf{r}). \quad (2.29)$$

At $r = r_{\max}$ Eq.(2.29) becomes

$$\Psi_{\gamma'}(\mathbf{r}_{\max}) = \sum_{\gamma} \mathcal{T}_{\gamma} (A_{\gamma\gamma'} H_{\ell_{\gamma}}^{(-)}(k_{\gamma} r_{\max}) + B_{\gamma\gamma'} H_{\ell_{\gamma}}^{(+)}(k_{\gamma} r_{\max})), \quad (2.30)$$

The inclusive penetrability of the Coulomb potential barrier for $r \leq r_{abs}$ is given by

$$P_J(E) = \sum_{\gamma} \frac{k_{\gamma}(r_{abs})}{k_0} |\mathcal{T}_{\gamma}^J|^2 \quad (2.31)$$

and the cross-section of fusion can be calculated as

$$\sigma_F(E) = \frac{\pi}{k^2} \sum_J (2J + 1) P_J(E), \quad (2.32)$$

where $k^2 = \frac{2\mu E_{cm}}{\hbar^2}$, μ is the reduced mass and E_{cm} is the incident energy.

Chapter 3

Fusion cross sections of ${}^{6,7}\text{Li}$ -induced reactions

In this chapter we study fusion cross sections of different reactions induced by ${}^{6,7}\text{Li}$ projectiles, for target masses ranging from light to heavy. Such reactions are widely investigated in the literature from both theoretical and experimental aspects (see for example Refs.[30, 31, 33, 34, 35, 36, 38, 40, 41, 42] and references therein). We start with the simple case of spherical nuclei (which is a one-dimensional potential model), where the convergence of the fusion cross sections for radial coordinates is analysed considering various target masses. The case where the targets are deformed will be also considered in order to analyse the effect of such deformation on the fusion cross section.

3.1 Case of spherical projectile and target nuclei

We first consider spherical colliding nuclei, meaning that no deformations nor internal structures of the interacting partners are taken into account. The radial coordinate between the centre of mass of the interacting particles is the only variable. We start with the description of the interacting potentials.

3.1.1 Description of fusion potentials

As mentioned before, the projectile-target fusion potential $V(r)$ is a sum of a nuclear term $[V_N(r)]$ and $[V_C(r)]$ a Coulomb term, $[V(r) = V_N(r) + V_C(r)]$. In order to numerically

solve Equation (2.5), the parameters of this potential are needed as inputs. In this work, we consider a Woods-Saxon shape for the nuclear part, whose parameters, i.e, the depth V_0 , radius r_0 , and diffuseness a_0 are summarized in Table 3.1. The nuclear radius R_0 , is given by $R_0 = r_0(A_P^{1/3} + A_T^{1/3})$, where A_P and A_T are projectile and target mass numbers, respectively. As indicated elsewhere, this potential is real due to the adopted incoming wave boundary condition. The references where these parameters were taken from are also indicated in this table. Apart from being induced by light loosely-bound projectiles, the choice of these reactions is also motivated by the availability of experimental data.

Table 3.1: Parameters V_0 , r_0 , and a_0 of the Wood-Saxon potential, for the different reactions considered. The reduced radii r_0 are converted to absolute ones as The nuclear radius is given by $R_0 = r_0(A_P^{1/3} + A_T^{1/3})$.

	${}^6\text{Li}$				${}^7\text{Li}$			
Nucleus	$V_0(\text{MeV})$	$r_0(\text{fm})$	$a_0(\text{fm})$	Ref	$V_0(\text{MeV})$	$r_0(\text{fm})$	$a_0(\text{fm})$	Ref
${}^{28}\text{Si}$	36.64	1.163	0.583	[41]	38.27	1.164	0.589	[36]
${}^{64}\text{Zn}$	45.81	1.174	0.614	[35]	42.79	1.170	0.606	[35]
${}^{152}\text{Sm}$	46.08	1.175	0.614	[31]	45.81	1.174	0.614	[30]
${}^{198}\text{Pt}$	47.37	1.176	0.618	[40]	45.81	1.174	0.614	[34]
${}^{209}\text{Bi}$	47.63	1.177	0.619	[38]	47.49	1.177	0.626	[33]

The different potentials, $V_N(r)$, $V_C(r)$ and $V(r)$ are plotted in Fig. 3.1. As one would expect, we notice in this figure that the nuclear potential being short-ranged, quickly vanishes at $r \geq R_0$. In this case, the total potential has only its Coulomb component in the asymptotic region [$V(r) \rightarrow V_C(r)$]. We also observe that the combination of the attractive nature of the nuclear potential and the repulsive nature of the Coulomb potential create a pocket in the total potential, which represents the minimum of the function $V(r)$, where this potential is most attractive. This attraction is responsible for the fusion reaction. In other words, two interacting systems can sit in this pocket for a long time, thus resulting in a fusion of both to form a compound system. The fusion process stops if this pocket disappears. This occurs for higher angular momenta when the sum of the Coulomb and centrifugal potentials override the attractive effect of the nuclear potential. .

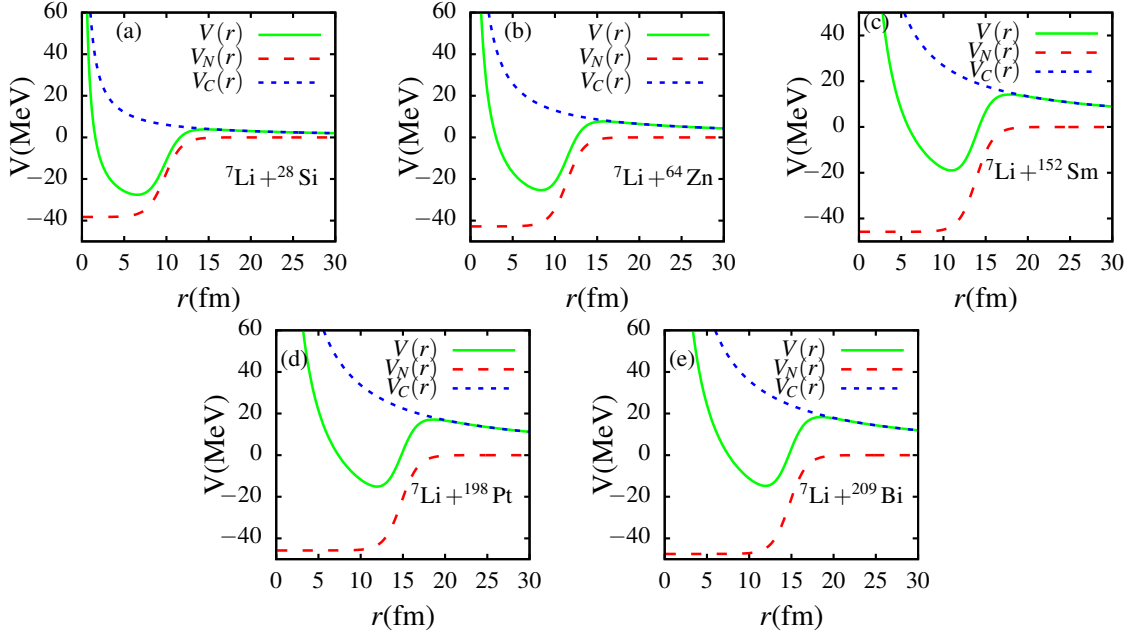


Figure 3.1: Plots of nuclear, $V_N(r)$, Coulomb $V_C(r)$, and total potentials $V(r)$, as functions of the radial distance (r), for different interacting systems.

A strong look at Fig.3.1 shows that the function $V(r)$ drops to its minimum, rises again to reach a relative maximum around R_0 , before it drops once. The maximum value to which it rises represents the Coulomb barrier height (V_B), and the value of r which corresponds to V_B , represents the barrier radius (R_B).

V_B and R_B are very important parameters in fusion reactions. In fact, based on this barrier, fusion reactions are classified in three types, depending on the incident energy E , below the barrier fusion ($E < V_B$), around the barrier fusion ($E = V_B$), and above the barrier fusion ($E > V_B$). Fusion dynamics below and above the Coulomb barrier are quite different. Although simpler theoretical approach fairly describe well the experimental data for incident energy above the Coulomb barrier, this has been shown not to be the case for energies below this barrier.

3.1.2 Convergence of fusion cross sections

In order to display the importance of the Coulomb barrier radius R_B in fusion reactions, we start by analysing the convergence of fusion cross sections as functions of the centre-of-mass incident energy with respect to the cut-off value of the radial numerical integration

parameter r_{\max} . The results obtained for ${}^6,{}^7\text{Li}$ projectiles are given in Fig.3.2. The value of the Coulomb barrier radius is indicated in each panel of these figures. As indicated in the previous chapter, the numerical calculations were carried out with the computer code CCFULL [45].

An inspection of each panel in these figures shows a rapid convergence of the fusion cross sections beyond R_B , for all reactions, since the contribution of $r_{\max} > R_B$ is practically negligible and this is independent of the target mass. These figures clearly show how the fusion cross section diminishes as interacting particles move away from each other towards the peripheral region. A numerical advantage of this analysis is that there is no benefit from an integration well beyond R_B ($r_{\max} \gg R_B$). Also, it is clear that values of r_{\max} slightly lower than R_B are not optimum to guarantee the convergence of the results. On the other hand, these figures indicate that values of r much larger than R_B are not needed to guarantee converged results.

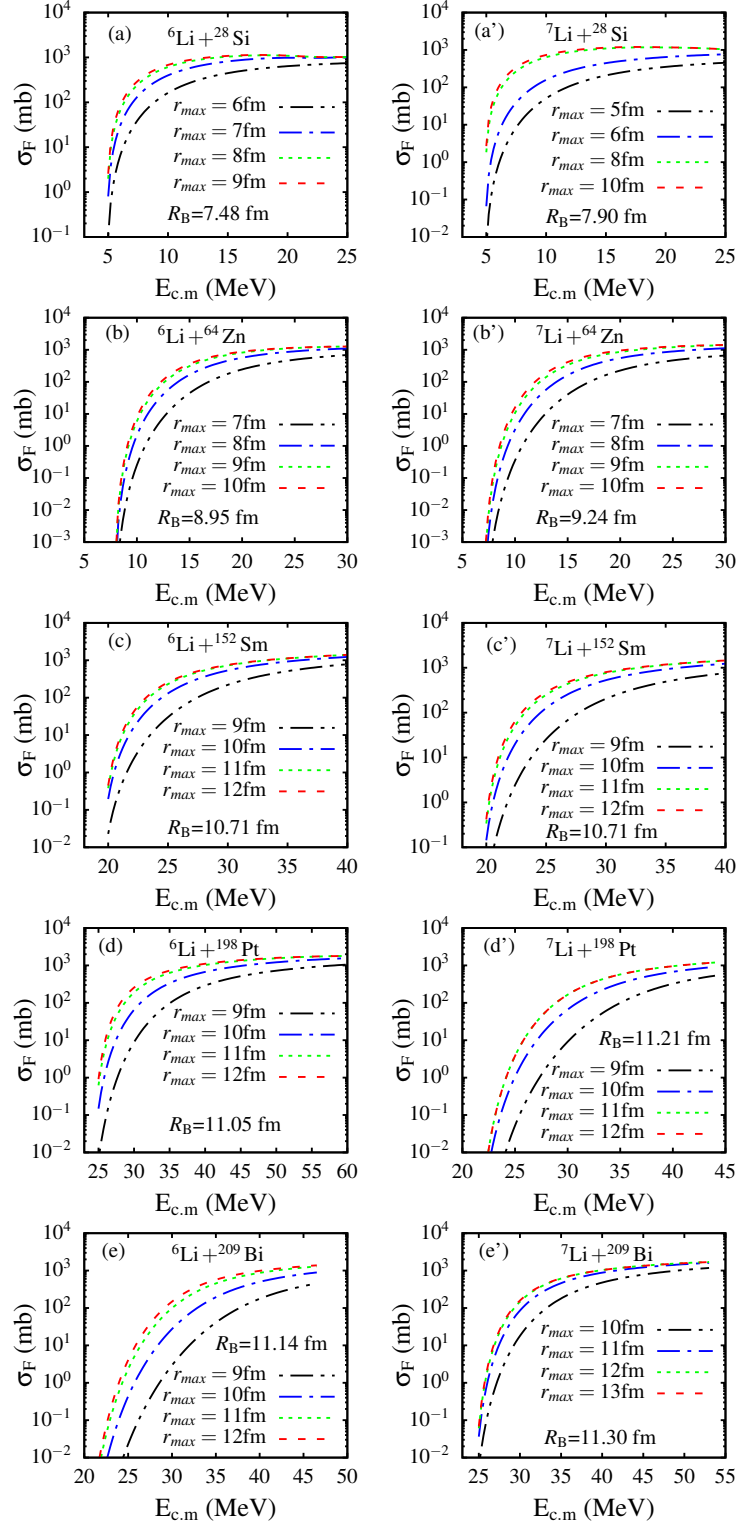


Figure 3.2: Convergence of the fusion cross sections as functions of the center-of-mass incident energy ($E_{c.m.}$), with respect to the numerical integration r_{max} , for ${}^6,{}^7\text{Li}$ projectiles

3.1.3 Comparison with the experimental data

In this section, we discuss the comparison of our theoretical fusion cross sections with the experimental data. Notice that a good convergence of the fusion cross sections obtained in Fig.3.2, does not necessarily imply that the calculations will provide a good description the experimental data. This comparison is displayed in Fig.3.3. The experimental data were obtained from Refs.[30, 31, 33, 34, 35, 36, 38, 40, 41], which are also repeated in the caption for each figure. Looking at these figures, we notice an excellent agreement between our theoretical calculations and the experimental data, regardless of the target mass. However, we notice a discrepancy for ^{152}Sm [panels (c) and (c')] where the calculations tend to overestimate the data. We recall that in these calculations, no target or projectile excitations were taken into account. It is therefore interesting to find that a simple one-dimensional potential model fits well the experimental data even at incident energies below the Coulomb barrier.

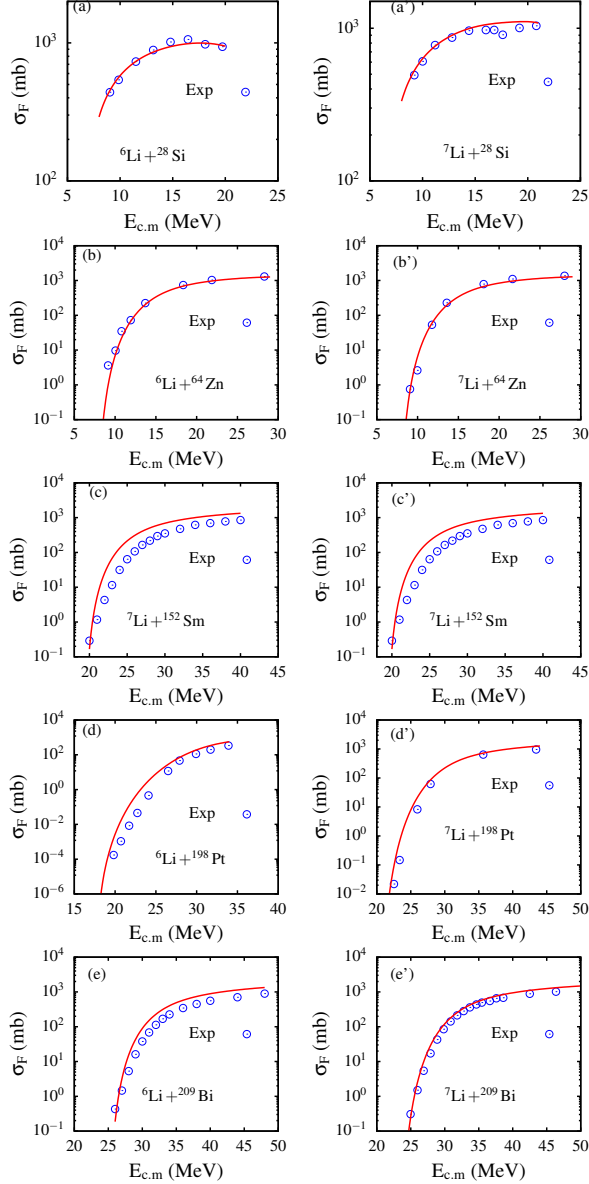


Figure 3.3: Comparison of the theoretical calculations with experimental data for ${}^6\text{Li}$ projectile. The data were obtained from [41], for ${}^{28}\text{Si}$, [35], for ${}^{64}\text{Zn}$, [31], for ${}^{152}\text{Sm}$, [40], for ${}^{198}\text{Pt}$ and [38], for ${}^{209}\text{Bi}$ target nuclei. The data were obtained from [36], for ${}^{28}\text{Si}$, [35], for ${}^{64}\text{Zn}$, [30], for ${}^{152}\text{Sm}$, [34], for ${}^{198}\text{Pt}$ and [33], for ${}^{209}\text{Bi}$ target nuclei.

3.2 Case of a deformed target

Given an excellent agreement between the theoretical calculations and the experimental data in Fig.3.3, one would wonder whether any deformation of the interacting partners would have any effects on the fusion cross sections. The targets considered in these figures

are known to be deformed, hence one would expect some effect, particularly for incident energies below the Coulomb barrier. In this work we only consider quadrupole (β_2) and hexadecapole (β_4) deformations, since higher-order deformations have not been found to account for any significant effect on fusion cross sections [12]. The different deformation parameters, β_2 and β_4 , obtained from Ref.[3], are summarized in Table 3.2.

Table 3.2: Potential deformation parameters of target nuclei under investigation obtained from Ref.[3].

	^{28}Si	^{64}Zn	^{152}Sm	^{198}Pt	^{209}Bi
β_2	-0.363	0.185	0.237	-0.115	-0.011
β_4	0.187	-0.024	0.097	-0.018	0.00
ϵ_2	-0.37	0.17	0.22	-0.11	-0.01
ϵ_4	-0.12	0.03	-0.06	0.02	0.00

We notice in this table that both ^{28}Si and ^{64}Zn have one negative and one positive deformation parameter, both parameters are positive for ^{152}Sm , they are both negative for ^{198}Pt , and $\beta_4 = 0$ for ^{209}Bi . In order to analyse the effect of these parameters on the fusion cross section, we will consider the case where each parameter is considered separately, and the case where they are both included in the calculations at the same time. However, before we consider the fusion cross section, we start with the potential $V(r)$.

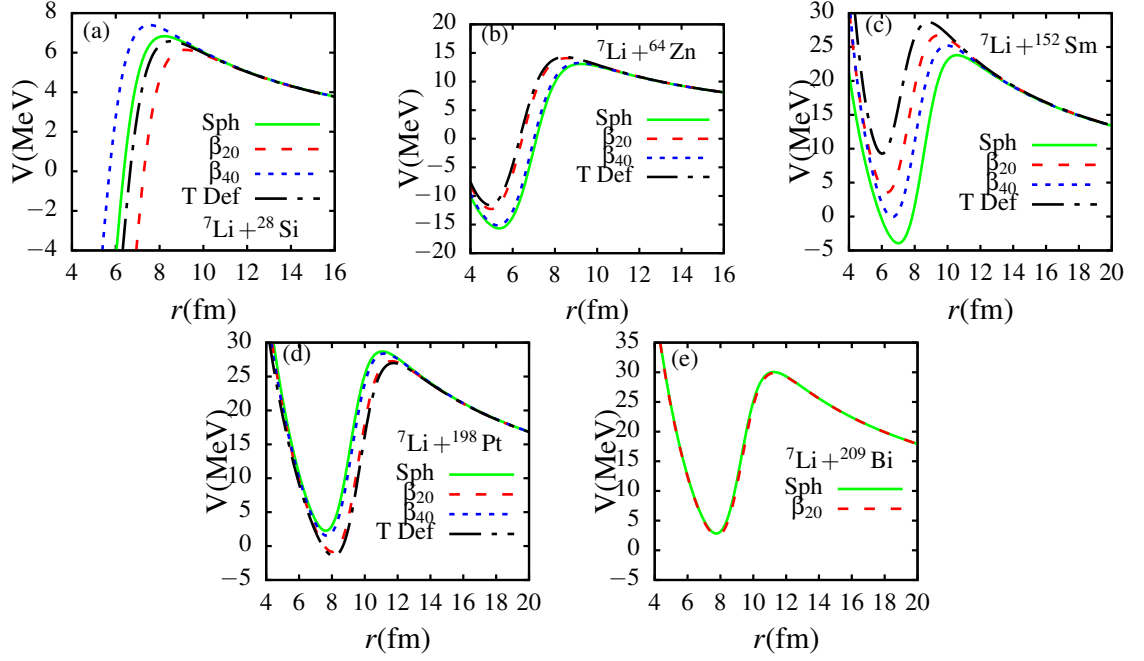


Figure 3.4: Plots of deformed total potential for different interacting systems. "Sph" represent a spherical target, i.e, when no deformations are included, "T Def" stands for target deformation, when both β_2 and β_4 are included simultaneously.

The effect of a target deformation is clearly noticed in Fig.3.4. We observe that a negative deformation parameter reduces the Coulomb barrier, whereas a positive one increases the Coulomb barrier. It is also obvious that the larger parameter corresponds to the most significant effect. Notice that lowering the Coulomb barrier results in an increase of the fusion cross section. In this case, one would then expect the negative deformation parameter to enhance the fusion cross section, while a positive one would produce a suppression of the fusion cross section. However, since we calculated potential only for $\theta = \pi$, it is not guaranteed that the fusion cross section will exhibit exactly the same pattern since it is calculated at different angles and not only only at $\theta = \pi$.

In Fig.3.5, the fusion cross sections calculated separately for β_2 and β_4 , and when both parameters are included simultaneously are shown. The spherical case (i.e., when $\beta_{20} = \beta_{40} = 0$) is also shown as in Fig.3.3. Observing this figure, we notice that the fusion cross sections calculated for both parameters separately are the same. However, when both parameters are combined, they suppress the fusion cross section for ^{28}Si [panels (a) and (a')] and for ^{152}Sm [panels (c) and (c')] targets. They rather enhance the fusion cross

sections for ^{64}Zn target at incident energies around and below the Coulomb barrier [panels (b) and (b')], whereas they have a negligible effect for ^{198}Pt target [panels (d) and (d')]. Another interesting observation is that now the experimental data are well fitted by the theoretical calculations in panels (c) and (c'), contrary to panels (c) and (c') of Fig.3.5. It follows that to better describe the experimental data for ^{152}Sm target, one needs to consider its deformation.

In conclusion, in this chapter we have considered fusion reactions of light loosely-bound projectiles on different target masses. A simple one-dimensional potential model provides a better fit of the experimental data, except for ^{152}Sm target where this target needs to be deformed in order to better fit the data. A study of the convergence of the fusion cross section in terms of the maximum radial numerical integration parameter r_{max} , shows a rapid convergence of the calculations for values of r_{max} around the Coulomb barrier radius, indicating that larger values than the barrier radius are irrelevant in the calculations. In order to get more insight into these results, in the next chapter, we consider fusion reactions induced by ^{40}Ca projectile.

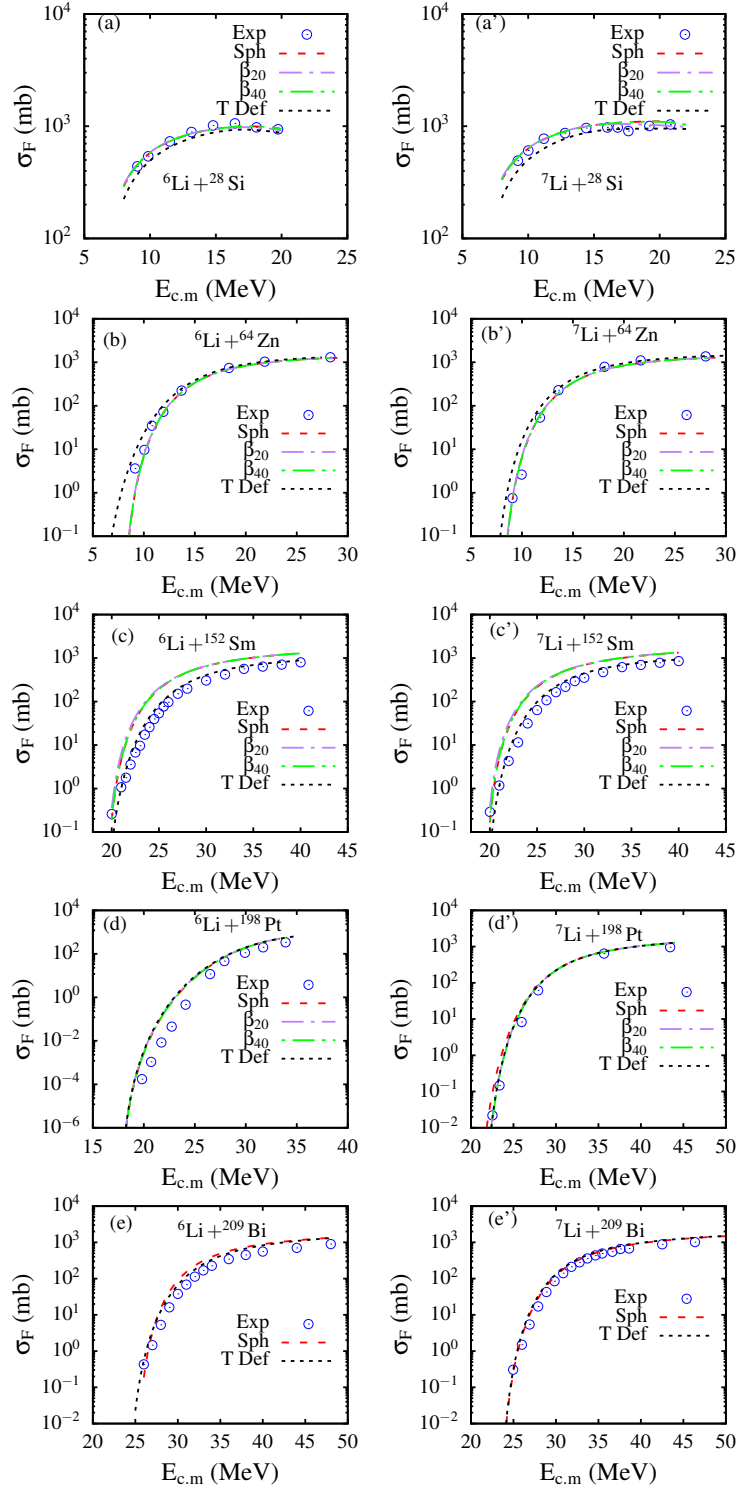


Figure 3.5: Fusion cross sections of ${}^6,{}^7\text{Li}$ projectiles on different target masses. For ${}^6\text{Li}$ projectile, experimental data were taken from [41] (${}^{28}\text{Si}$), [35] (${}^{64}\text{Zn}$), ${}^{152}\text{Sm}$ [31], ${}^{198}\text{Pt}$ [40] and ${}^{209}\text{Bi}$ [38]. For ${}^7\text{Li}$ projectile, they were taken from ${}^{28}\text{Si}$ [36], ${}^{64}\text{Zn}$ [35], ${}^{152}\text{Sm}$ [30], ${}^{198}\text{Pt}$ [34] and ${}^{209}\text{Bi}$ [33].

Chapter 4

Fusion cross sections of ^{40}Ca -induced reactions

In this chapter we discuss fusion cross sections induced by ^{40}Ca the projectile. As target nuclei, we consider ^{62}Ni , ^{64}Ni , ^{96}Zr , ^{194}Pt , and ^{238}U . The interaction of this projectile with the last target can be regarded as leading to a formation of superheavy elements, that is $^{40}_{20}\text{Ca} + ^{238}_{92}\text{U} \rightarrow ^{112}_{112}\text{X}^{278}$. As in the previous chapter where light projectiles $^6,^7\text{Li}$ were considered, we adopt the same approach, and start with the simple case of one-dimension potential model, where the interacting partners are considered to be inert, meaning that no projectile and target excitations are considered (Section 4.1). We will when analyse the effect of the target quadrupole β_2 and hexadecapole β_4 deformations on the fusion cross sections (Section 4.2). Analyzing the effects of these two parameters in the previous chapter, we found that for the ^{152}Sm target where both β_2 and β_4 are positive, their effect was observed to suppress the fusion cross section, mainly at energies below and around the Coulomb barrier. On the other hand, for ^{28}Si and ^{64}Zn , where one of these parameters is negative, we found that their effect is to enhance the fusion cross section in the same incident energy range. In this chapter, we will also investigate the effect of these parameters on fusion cross section in ^{40}Ca -induced reactions [18, 20, 21, 22, 24]. In Section 4.4, we will consider the effect of neutron transfer channels on the fusion cross section. Again, the choice of these reactions are informed by the availability of the experimental data.

4.1 Case of spherical projectile and target nuclei

As the nucleus-nucleus potential is the main input in our calculations, for each target, we summarize the parameters V_0, r_0 and a_0 of the nuclear potential in Table 4.1. The references where these parameters were obtained are also indicated in this table.

Table 4.1: Parameters V_0, r_0 , and a_0 of the ^{40}Ca -target nuclear potentials. The absolute radii are obtained from the reduced one (r_0) as $R_0 = r_0(A_p^{1/3} + A_t^{1/3})$.

Target	$V_0(\text{MeV})$	$r_0(\text{fm})$	$a_0(\text{fm})$	Ref
^{62}Ni	68.283	1.176	0.663	[18]
^{64}Ni	68.699	1.176	0.664	[20]
^{96}Zr	73.979	1.177	0.673	[21]
^{194}Pt	82.897	1.180	0.686	[22]
^{238}U	85.402	1.181	0.689	[24]

4.1.1 Convergence analysis

The different fusion cross sections calculated within the one-dimensional potential model are shown in Fig.4.2. The value of the Coulomb barrier radius is indicated in each panel. Inspecting this figure, we notice that the fusion cross sections convergence rapidly for $r_{\text{max}} \geq R_B$, similar those in Fig.3.2, for light projectiles ($^{6,7}\text{Li}$)-induced reactions. For example, one can quickly deduce that for ^{62}Ni target, the convergence is obtained for $r_{\text{max}} = R_B + 0.085R_B$, for $r_{\text{max}} = R_B + 0.114R_B$ (^{96}Zr target) and for $r_{\text{max}} = R_B + 0.177R_B$ (^{238}U). Again, it follows that higher values of r_{max} well beyond R_B are not necessary in order to achieve the convergence of fusion cross sections even in ^{40}Ca -induced fusion reactions.

The convergence of the fusion cross section means that for the maximum value of r_{max} where the convergence is obtained, the Coulomb and centrifugal barriers have already canceled the effect of the nuclear potential. In other words, there is no more Coulomb pocket that is responsible for fusion. In order to verify this, we first define the angular

momentum (ℓ) from a classical point of view as

$$\ell = kr \Rightarrow \ell_{\max} = kr_{\max}, \quad (4.1)$$

where $k = \sqrt{2\mu E_{\text{c.m.}}/\hbar^2}$ has been defined as the wavenumber. In this case, the centrifugal barrier corresponding to ℓ_{\max} is given by

$$V_{\text{cent}}(r) = \frac{\ell_{\max}(\ell_{\max} + 1)}{2\mu r^2}. \quad (4.2)$$

The values of r_{\max} , k , and ℓ_{\max} are given in Table 4.2. Obviously in this table, we notice that these parameters increase with the target mass. In Fig.4.1, we plot the potential $V(r) = V_N(r) + V_C(r) + V_{\text{cent}}(r)$, for different values of the orbital angular momentum (ℓ), only for ^{64}Zn and ^{238}U . Indeed, one sees in this figure that the Coulomb pocket, which is responsible for the fusion process has already disappeared for $\ell = 100$, even for ^{238}U target, which implies a negligible contribution to the fusion cross section beyond ℓ_{\max} , as demonstrated in Fig.4.2.

Table 4.2: Values of the maximum integration parameter (r_{\max}), wavenumber (k), and maximum angular momentum (ℓ_{\max}), obtained from Eq.(4.1), for the different targets considered. The wave-number was calculated at $E_{\text{c.m.}} = V_{\text{B}}$.

Target	^{62}Ni	^{64}Ni	^{96}Zr	^{194}Pt	^{238}U
r_{\max}	11.0	11.0	12.0	14.0	14.0
k	9.61	9.89	12.02	17.36	19.1
ℓ_{\max}	106	109	144	208	229

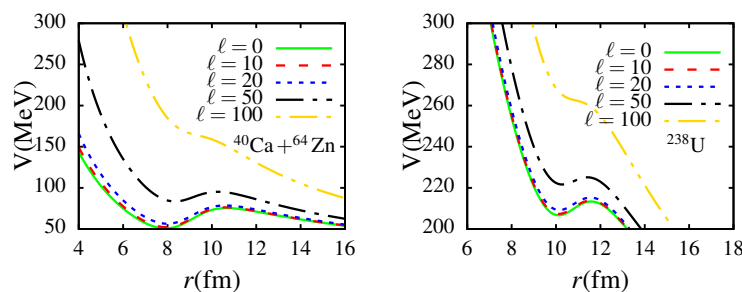


Figure 4.1: Effect of angular momentum ℓ on the Coulomb pocket.

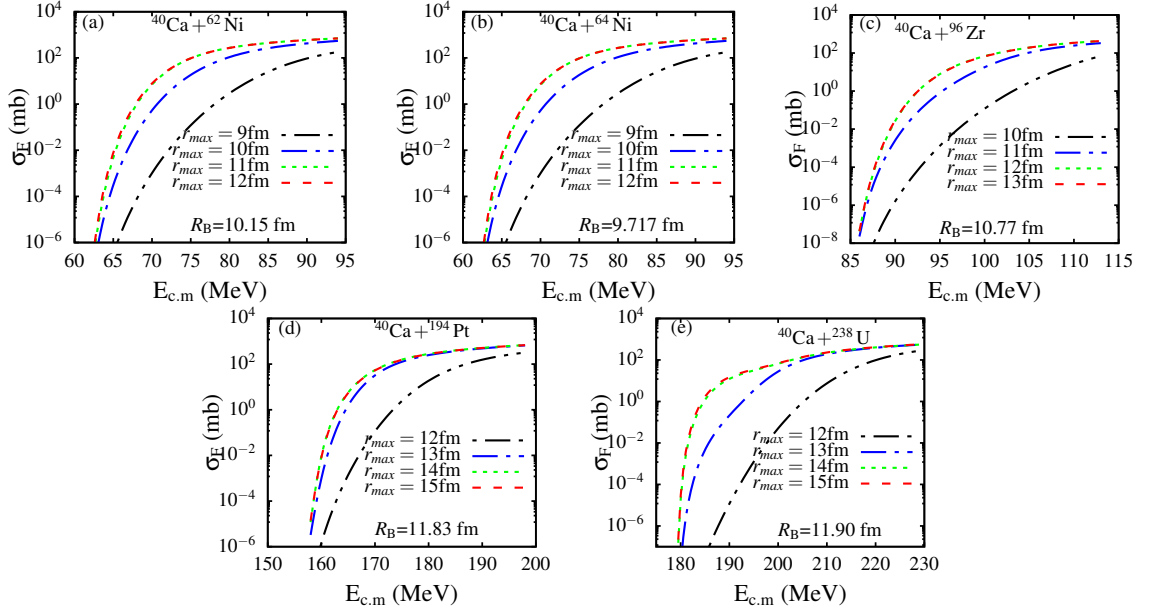


Figure 4.2: r_{max} convergence for heavy-heavy fusion reaction.

4.1.2 Comparison with experimental data

In the previous chapter, we have seen that the target deformations are not that needed if one is interested in fitting the experimental data for fusion reactions induced by light ${}^{6,7}\text{Li}$ projectiles, except in the case of ${}^{6,7}\text{Li}+{}^{152}\text{Sm}$ reactions, where both β_2 and β_4 deformation parameters are crucial in fitting the data. In the case of ${}^{40}\text{Ca}$, we do not expect the simple one-dimensional potential model to fit the data, considering the large mass of this nucleus compared to that of ${}^{6,7}\text{Li}$ nuclei. To show the limitation of this model in this case, we compare, in Fig.4.3, our results with the experimental data. The data were obtained from [18] (${}^{62}\text{Ni}$), [20] (${}^{64}\text{Ni}$), [21] (${}^{96}\text{Zr}$), [22] (${}^{194}\text{Pt}$), and [24] (${}^{238}\text{U}$). Observing this figure, it follows as expected, that the theoretical calculations are in agreement or tend to agree with the data at incident energies above the Coulomb barrier. It is well known that in this incident energy region, the internal structures of the interacting systems play a minor role in the fusion process. This is due to small effects of the Coulomb barrier, owing to a weak Coulomb repulsion, resulting in a large amount of flux tunnelling through the barrier to account for the fusion cross section. However, below the Coulomb barrier, where the Coulomb repulsive is stronger, a sharp disagreement is observed, where the theoretical calculations largely underestimate the experimental data, and this appears

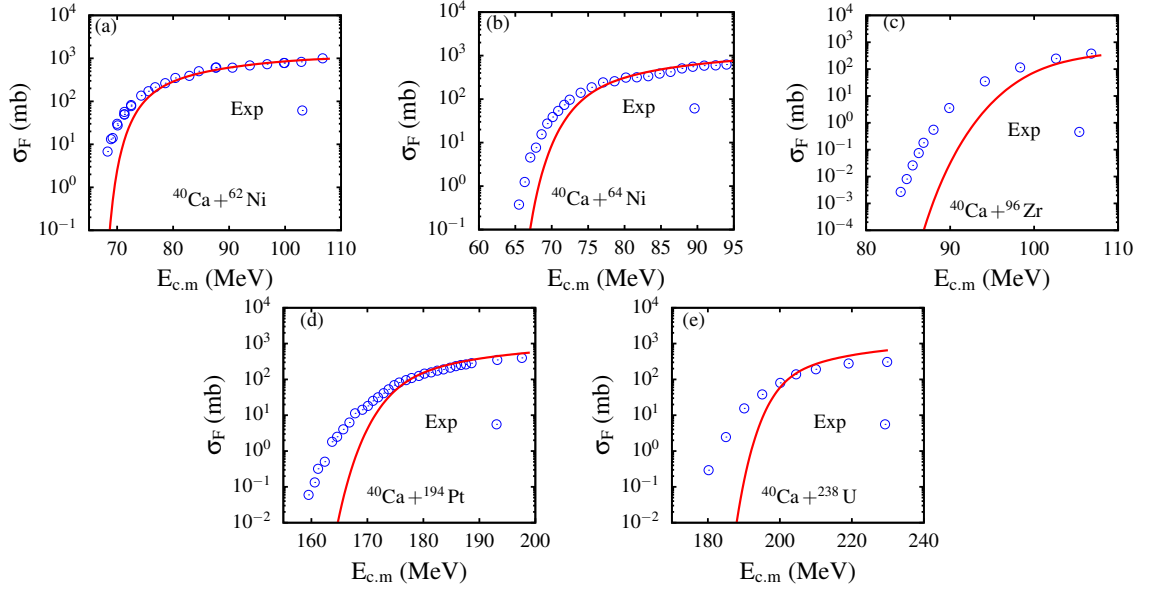


Figure 4.3: Comparison of the fusion experimental data with the one-dimensional potential model, in reactions induced by ^{40}Ca projectile. The experimental data taken from Ref.[18] for ^{62}Ni , [20] for ^{64}Ni , [21] for ^{96}Zr , [22] for ^{194}Pt and [24] for ^{238}U .

to deepen as the target mass increases. This substantial suppression of the fusion cross section is therefore attributed to a strong Coulomb repulsion and large Coulomb barrier compared to the incident energy, which significantly reduces the flux that tunnels through the barrier. This means that reaction mechanisms or channels that can contribute to lower the Coulomb barrier in order to enhance the fusion cross sections are needed to describe the experimental data. In the next section, we discuss different reaction mechanisms that would enhance the fusion cross section at energies below the Coulomb barrier, starting with the deformation of the target.

4.2 Deformation of the target nucleus

In this section, we analyse the effect of the target deformation on the fusion cross section. In Fig.3.5, we have seen that the target deformation parameters β_2 and β_4 , can either suppress or enhance the fusion cross section. As before, we start with the analysis of the effect of these parameters on the interacting potential. The deformation parameters for each target were taken from Ref.[3], and are summarised in Table.4.3. According to

[3], for ^{40}Ca isotope $\beta_2=\beta_4=0.0$

Table 4.3: Deformation parameters and associated energies for $^{62,64}\text{Ni}$, ^{96}Zr , ^{194}Pt and ^{238}U obtained from Ref [3].

	^{62}Ni	^{64}Ni	^{96}Zr	^{194}Pt	^{238}U
β_2	0.107	-0.094	0.240	0.130	0.236
β_4	-0.020	-0.008	0.011	-0.055	0.098
ϵ_2	0.10	-0.09	0.22	-0.11	0.22
ϵ_4	0.02	0.01	0.01	0.02	-0.06

Fig.4.4 shows the deformed potential $V(r)$, for each target. In this figure, the label "Sph" represents the case of spherical target, i.e., where $\beta_2 = \beta_4 = 0$. β_2 , represent the case where only β_2 parameter is included in the calculations, β_4 shows data where only β_4 parameter is included and label "T Def" represents the case where both β_2 and β_4 parameters are included in the calculation. A closer look at this figure reveals that the effect of β_2 is to increase the Coulomb barrier height except for ^{64}Ni target, where it has a negative value. It is clear from this figure that a negative value of the deformation parameter lowers the Coulomb barrier height. A further observation of this figure shows an important effect when both parameters are combined in the calculations, particularly for heavy targets. We notice that the inclusion of both parameters favours the effect of the parameter with a higher numerical value.i.e, for the reaction including $^{40}\text{Ca} + ^{194}\text{Pt}$ (panel d), $\beta_2 = 0.13$ and $\beta_4 = -0.055$ therefore "T-Def" will take the effect of the positive β_2 . We need to mention that we only considered the case where $\theta = \pi$.

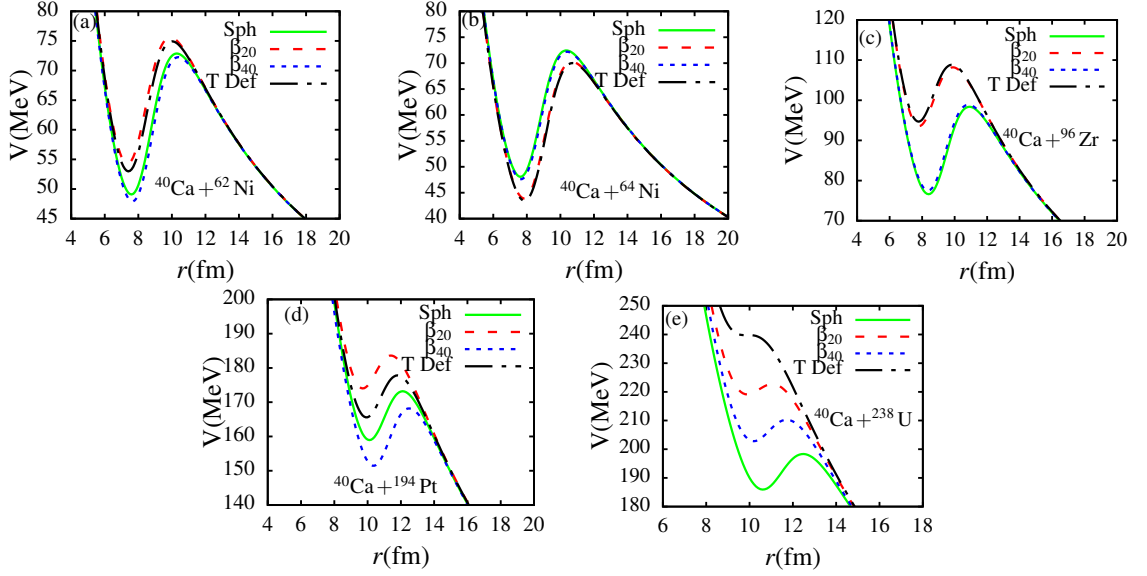


Figure 4.4: Deformed total potential for heavy-heavy collision systems. 'Sph' corresponds to spherical target where no deformations are included. The label 'T Def' is the deformed target where both β_2 and β_4 have been included and the labels β_2 and β_4 corresponds to calculations where only β_2/β_4 deformations are included.

Having analyzed the effect of the deformation parameters on the Coulomb barrier height, let us now investigate how they affect the fusion cross sections. To this end, we plot in Fig.4.5, the fusion cross sections corresponding to separate β_2 and β_4 parameters, as well as when they are combined. The results of Fig.4.3 are repeated for a better comparison. Inspecting this figure, we notice that for Nickel targets [panels (a) and (b)], the target deformations have practical no effect on the fusion cross section as all different curves are hardly distinguishable. However, a clear enhancement of the fusion cross section due to these parameters is observed in panels (c), (d) and (e). It is further observed that the effect of β_2 is approximately similar to that of both parameters combined, whereas the effect of β_4 alone can be regarded as negligible since it is similar to the spherical case. However, one notice that while the target deformations effect play an important role, they still do not provide a better description of the experimental data at incident energies below the Coulomb barrier. It is therefore clear that other reaction mechanisms are needed besides these deformations in this incident energy region.

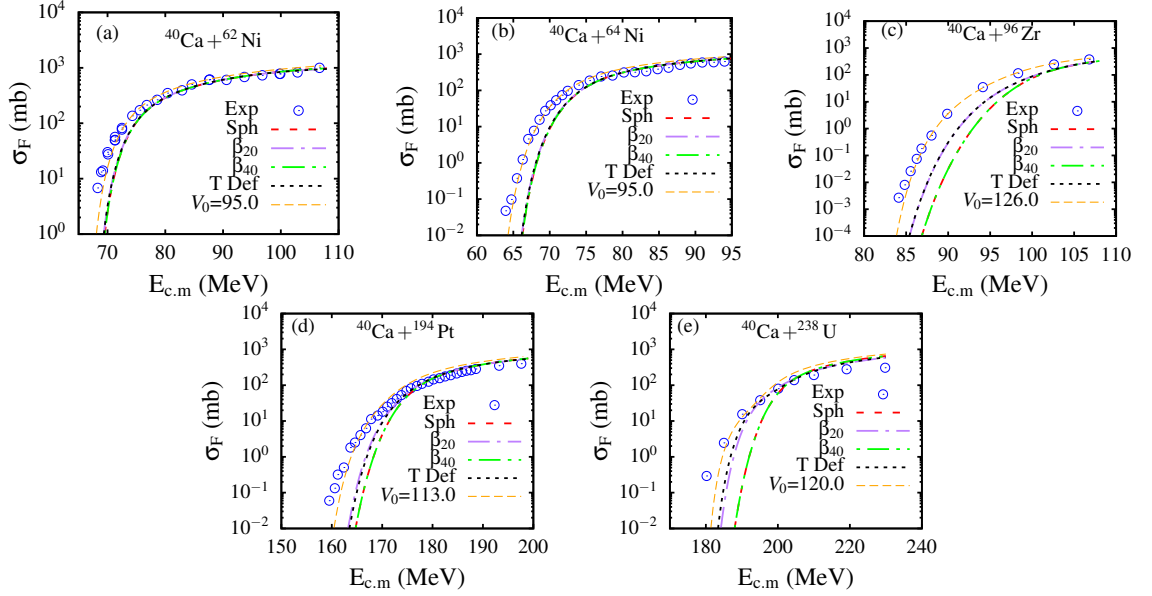


Figure 4.5: Fusion cross sections in reactions induced by ^{40}Ca projectile, obtained when target deformations are included in the calculations. The experimental data taken Ref.[18] for ^{62}Ni , [20] for ^{64}Ni , [21] for ^{96}Zr , [22] for ^{194}Pt and [24] for ^{238}U .

Notice that the potential parameters in Table.4.1, used to calculate the fusion cross sections are independent of the incident energy, meaning that they are the same below and above the Coulomb barrier. An energy dependent Woods-Saxon potential (EDWSP), where the potential parameters are dependent on the incident energy has been shown to better describe the fusion experimental data along with the target excitations (see for example Refs.[20, 55, 42]). In order to test whether this approach could improve the agreement between our calculations and the experimental data, we adjusted the depth V_0 , while other parameters R_0 and a_0 remained unchanged. Looking at this figure, it is remarkable to how this procedure agrees perfectly with the experimental data, even for heavy target nuclei. In panels (a) and (b), we observe that the value of V_0 that fits the data is independent of the target mass for isotopes of the same nucleus. It could be interesting to consider more isotopes in this regard. From panels (c)-(e), it follows that the value of V_0 is not proportional to the target mass. For ^{96}Zr , $V_0 = 126$ MeV, ^{194}Pt it is $V_0 = 113$ MeV and 120 MeV for ^{238}U target. Therefore, it could be equally interesting to investigate what makes V_0 increase or decreases in this case. This procedure of adjusting V_0 was also adopted in Ref.[53], for nuclear astrophysical reactions. It follows that the

depth of the Woods-Saxon potential plays an crucial role at incident energies below the Coulomb barrier.

4.3 Effects of vibration

Another channel to consider in the nuclear intrinsic state is the vibrational band. Figure.4.6 displays the vibrational effects on fusion in comparison to the rotational effects shown in figure.4.5. The deformation parameters for vibrational coupling are listed in Table.4.4. Vibrational coupling enhances fusion in Nickel and Platinum targets. This may be due to the group characteristics of the nuclei or the higher values of their vibrational parameters. For ^{96}Zr and ^{238}U , the vibrational modes of the targets hinders fusion when compared to the rotational effects. We notice that the 2 systems have their deformation parameters $\hbar\omega$ or β_λ at a value less than 0.1. Therefore, we can link the fusion hindrance in the target vibrational band to the values of $\hbar\omega$ and β_λ . In the next section we analyse effects of the nucleon transfer channel.

Table 4.4: Deformation parameters used in vibrational coupling for $^{62,64}\text{Ni}$, ^{96}Zr , ^{194}Pt and ^{238}U targets.

	^{62}Ni	^{64}Ni	^{96}Zr	^{194}Pt	^{238}U
$\hbar\omega$	1.1729	1.3458	1.7505	0.3285	0.0449
Ref	[18]	[20]	[21]	[22]	[24]

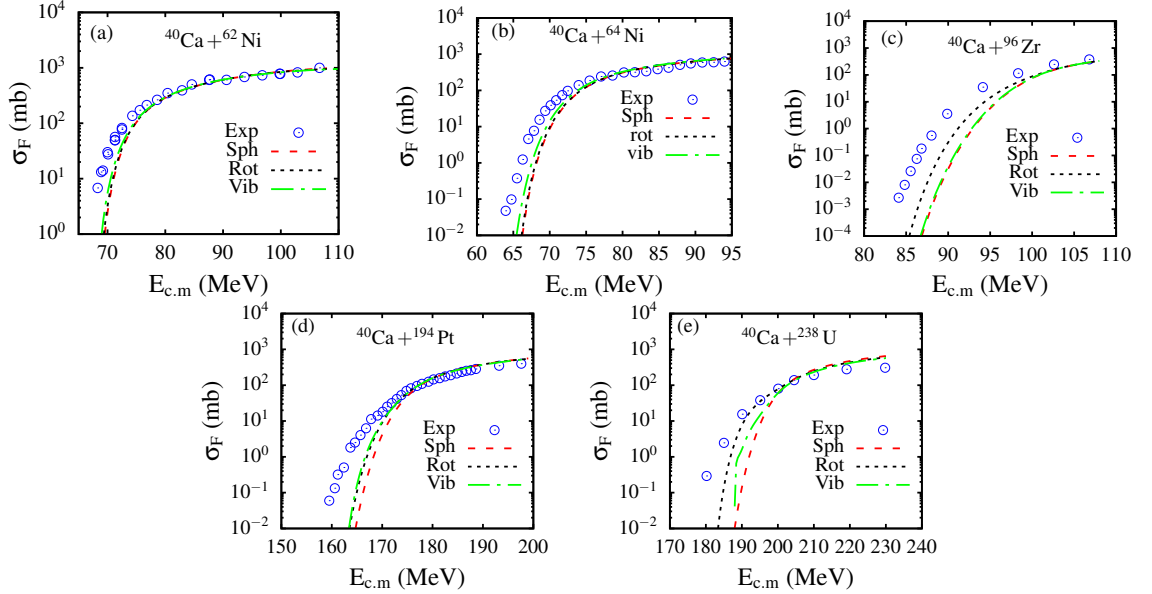


Figure 4.6: Effects of target vibration on fusion compared to rotational deformation and inert data.

4.4 Multi-neutron transfer effects

In the previous sections, we have discussed in detail the effect of target excitations on the fusion cross section. In this section, we focus our attention on the multi-neutron transfer effect. As we have already indicated in the introduction, this effect has been proven to be important on fusion cross section, and mainly depends on the Q-value of the reaction. We follow Refs.[42], and define the transfer channel as

$$F_{tr} = F_t \frac{dV_N}{dr}, \quad (4.3)$$

where F_t is a coupling strength which is adjusted to fit the experimental data and dV_N/dr is the first derivative of the nuclear potential. In this work, F_t has been set to a constant value of 0.5 as in Ref. [42]. In Table 4.5 we summarize the Q-values for +1n, +2n and +3n neutron transfers, for each reaction. We notice in this table that the Q-value is negative for +1n and +3n transfers for $^{40}\text{Ca}+^{62}\text{Ni}$ reaction, and also for +1n transfer for $^{40}\text{Ca}+^{64}\text{Ni}$. Elsewhere, the Q-value is positive. Fig.4.7, shows the fusion cross sections for +1n, +2n and +3n neutron transfer channels. Observing this figure, it resorts that at sub-barrier energies, the fusion cross sections are almost similar for all three transfer channels. For energies around the Coulomb barrier, we notice that the negative Q-value

Table 4.5: Q-values (MeV) for neutron transfer in various heavy ion systems of ^{40}Ca projectiles.

system	+1n	+2n	+3n	Ref
$^{40}\text{Ca} + ^{62}\text{Ni}$	-2.23	1.43	-2.03	[18]
$^{40}\text{Ca} + ^{64}\text{Ni}$	-1.30	3.35	0.69	[20]
$^{40}\text{Ca} + ^{96}\text{Zr}$	0.51	5.53	5.24	[21]
$^{40}\text{Ca} + ^{194}\text{Pt}$	0.01	5.23	4.50	[22]
$^{40}\text{Ca} + ^{238}\text{U}$	2.21	8.56	9.95	[24]

enhances the fusion cross section, and provides a better fit of the experimental data [see panels (a) and (b)], where +1n and +3n curves are hardly distinguishable. It is clear from panels (a) and (b) and the positive Q-value suppresses the fusion cross section. This suppression increases with the increase of the Q-value. This trend is maintained in panels (c), (d) and (e), where one also notices that the lower Q-value enhances the fusion cross section and provides a better fit of the data at energies around and above the Coulomb barrier. We further observe in panel (e) that all transfer channels underestimate the fusion cross section at sub-barrier energies.

In conclusion, multi-neutron transfer channels exhibit an important effect on the fusion cross section for energies around and above the Coulomb barrier. As far as the results in Fig.4.7 are concerned, the multi-neutron transfer channel does not appear to account for an meaningful effect at sub-barrier energies. A negative Q-value enhances the fusion cross section, whereas a positive one suppresses it.

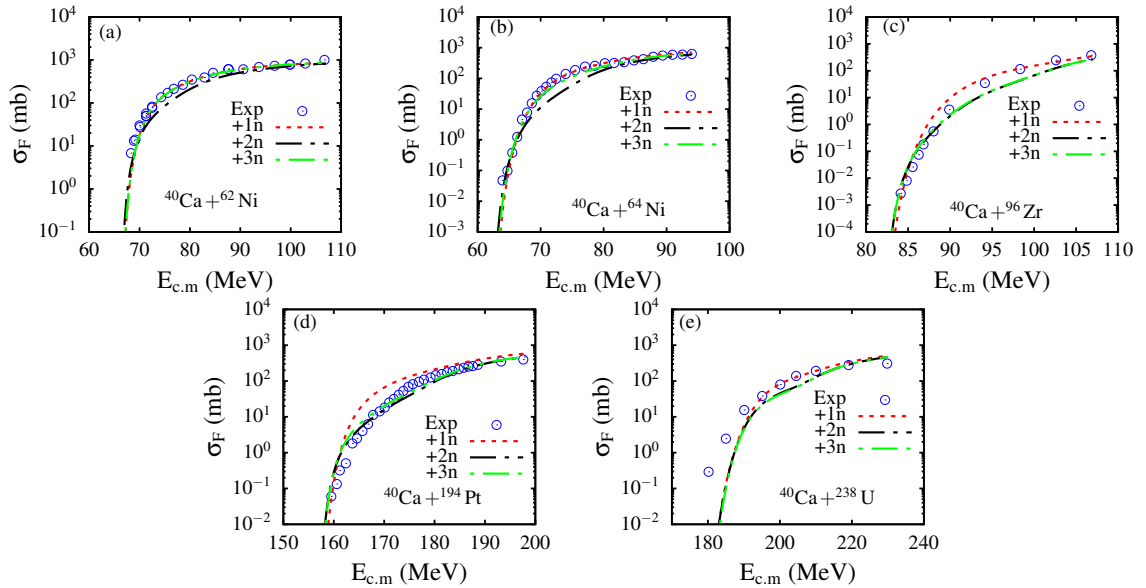


Figure 4.7: Effects of +1n, +2n and +3n transfer channels on fusion cross sections. The experimental data for ^{62}Ni , ^{64}Ni , ^{96}Zr , ^{194}Pt and ^{238}U are obtained from Refs.[18, 20, 21, 22, 24] respectively.

4.5 Fusion barrier distribution

In order to further investigate the target excitations and multi-neutron transfer channel effects on the fusion cross section, we consider the barrier distribution. It is well-known that one of the important features of the coupling channels, is to split the nominal Coulomb barrier of the interacting partners into multiple barriers with various degrees of penetrability associated with each barrier. For more details on this subject, one can consider Refs.[13, 16, 43, 64, 68, 72, 73, 74, 77, 78, 79, 80]. Following Ref.[43], we define the fusion barrier distribution as follows

$$D(E) = \frac{1}{\pi R^2} \frac{d^2(E\sigma)}{dE^2}, \quad (4.4)$$

where R is the barrier radius, E , the incident energy and σ , the fusion cross section. In this section, we consider not only the effect of multi-neutron transfer channels on the fusion barrier distributions but also the effect of target excitations. We have seen in the previous section that multi-neutron transfer channels mainly affect the fusion cross section around the Coulomb barrier. We then expect the fusion barrier distribution to clearly reflect the effect of multi-neutron transfer channels. In Fig.4.8, we start with the effect of the target

deformations (β_2 and β_4). Again, we consider the case of spherical target, represented by the curve "Sph". Starting with Nickel targets (which are lighter), we observe that the ^{62}Ni exhibits a broader distribution compared to ^{64}Ni target. We also observe that the inclusion of β_2 deformation appears to slightly shift the barrier distribution peak towards lower energies. This is more clear in panel (a). Considering ^{96}Zr target [panel (c)], we notice that although the barrier distributions corresponding to the spherical and β_4 cases still represents one peak around 98 MeV, the inclusion of β_2 displays a completely different picture. We first notice a complete suppression of the distribution peak around 98 MeV, with two peaks around 95 MeV and 100 MeV. The same trend is maintained in panel (d) for ^{194}Pt target. The only difference is that now curves corresponding to β_2 and "T Def" where the β_2 and β_4 are combined simultaneously are now different. It is interesting to observe that even though β_4 alone does not have any meaningful effect (since it is similar to the spherical case), its combination with β_2 results in an enhancement of the peak around 170 MeV, and its suppression around 176 MeV. For the heavier target (^{238}U), the effect of target deformation on the fusion barrier distribution is even more pronounced. Again β_4 alone does not affect the barrier distribution. We notice that combining both β_2 and β_4 produces an oscillatory barrier distribution.

The Common trend in these results is that in the case of spherical targets and when only β_4 deformation is included, the fusion barrier distribution contains only one peak. For the light targets (^{62}Zn and ^{64}Zn), these peaks are located exactly at energies corresponding to the nominal Coulomb barrier height (which is shown in each panel by a down-pointing arrow). However, in panels (c)-to (e), we observe that this peak is located past the nominal Coulomb barrier height, particularly as the target mass increases. The fact that peak of the spherical target is located beyond the nominal Coulomb barrier height as the target mass increases, is an interesting observation. As the barrier height increases, the fusion cross section is suppressed in particular at sub-barrier incident energies. As we have seen in Fig.4.3 for example, the one-dimensional potential model (which corresponds to the case of spherical target) underestimates the experimental data, and this becomes dramatic as the target mass increases. We can then relate this to the shift in the Coulomb barrier height toward larger values in Fig.4.8. Now, when β_2 deformation is included, we observe

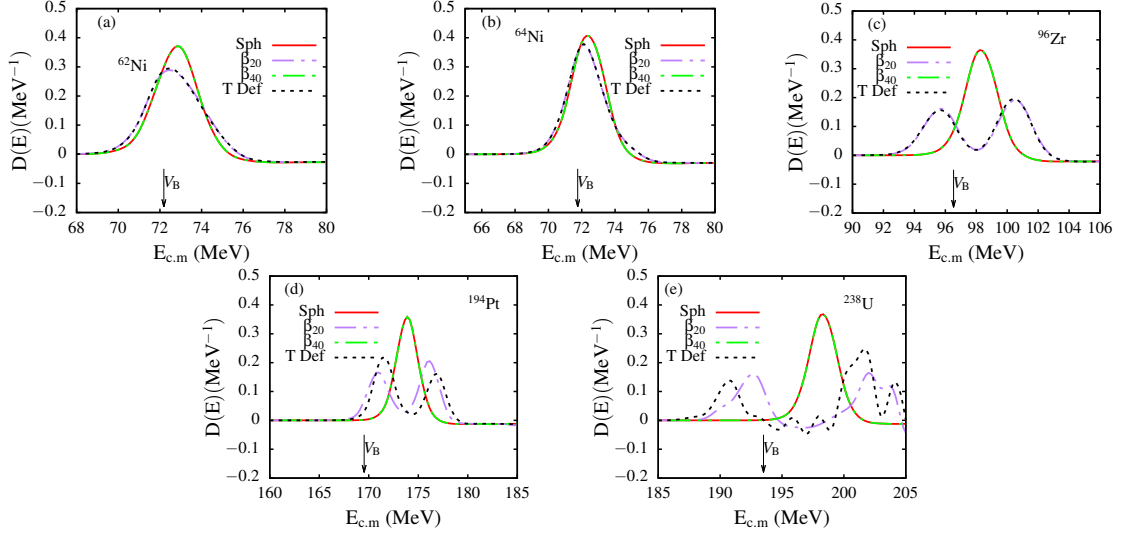


Figure 4.8: Effect of target β_2 and β_4 deformations on the fusion barrier distributions for ^{40}Ca -induced reactions. Label "Sph" represents the data for spherical collision where the deformation parameters are set to zero. "T Def" represents the data where both β_2 and β_4 parameters are considered.

in Fig.4.8 (c)-4.8(e) that the nominal barrier has been split into multiple barriers, with some of the barriers being located before the nominal Coulomb barrier height, and others beyond. The appearance of peaks below the nominal Coulomb barrier height attests to the fact that the deformation or excitations of target nucleus reduces the Coulomb barrier height through couplings to these states. Reducing the Coulomb barrier height produces the enhancement of the fusion cross section. This is exactly what we observe for example in Fig.4.5. To further emphasise this, we consider the ^{238}U target [panel (e)], where we notice that the peak corresponding to the combination of β_2 and β_4 "T Def" is further shifted to a lower incident energy compared to the case where only β_2 is included. Now, considering Fig.4.5, we can see that at incident energies below and around the Coulomb barrier, indeed the fusion cross section corresponding to "T Def" is lightly larger than that corresponding to β_2 alone. How about the barrier distribution peaks that are located beyond the nominal Coulomb barrier height? Since they correspond to barrier heights that are larger than the nominal one, they cannot be associated with the enhancement of the fusion cross section. They are rather expected to suppress the fusion cross section. This is actually what transpires in Fig.4.5 For example, from a careful look at Fig.4.5(e),

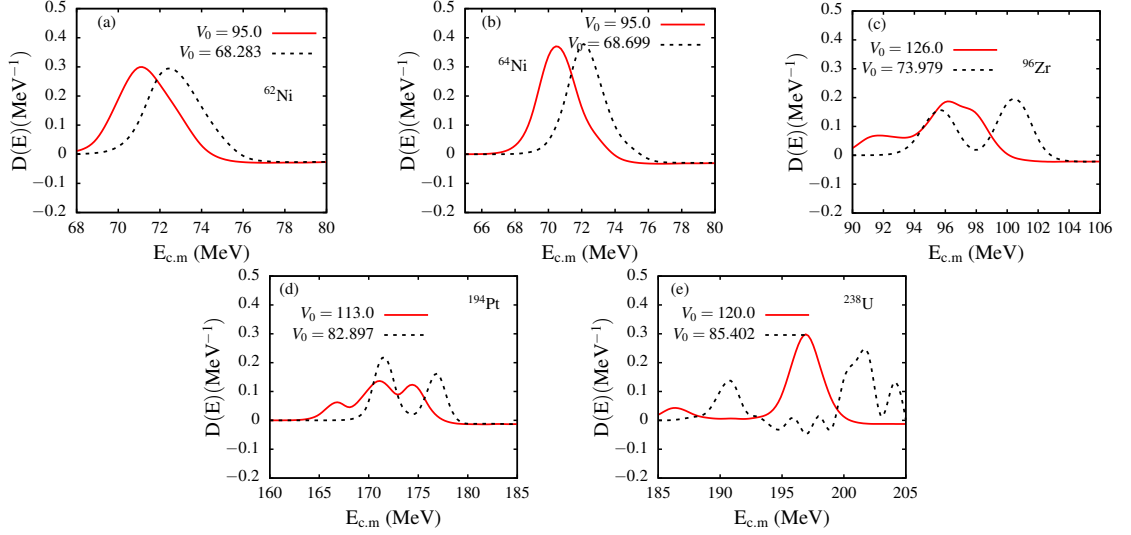


Figure 4.9: Comparison of fusion barrier distribution data for V_0 given in Table.4.1 and V_0 given in Fig.4.5 that agrees with the experimental data.

it follows that the fusion cross section is suppressed owing to the deformation of the target at incident energies above the Coulomb barrier.

As we have shown in Fig.4.5, at incident energies below and around the Coulomb barrier, the experimental data are excellently fitted with a larger value of the depth V_0 of the potential. Here we propose to verify how increasing the value of V_0 affects the barrier distributions. Based on our discussion above, since in this case the fusion cross section is enhanced, we expect the peak of the barrier distribution to further shift to lower energies. In Fig.4.9, we compare the fusion barrier distributions obtain with the V_0 values given Table 4.1 with the ones obtained using the larger V_0 values given in the different panels of Fig.4.5. Indeed, we notice that for the larger value of V_0 , the peak of the barrier distribution is shifted to lower energies, which amounts to the reduction of the Coulomb barrier height. We interestingly note that the second peaks on the right in panels (c)-(e) are completely washed away. One the other hand, the results obtained for the larger values of V_0 are more similar to those obtained in the case of spherical nuclei, but with peaks at lower energies.

A further discussion of these results, we show in Table 4.6, we record the positions of the

Table 4.6: Fusion barrier distribution peak positions displayed in Fig.4.9. V_B is the nominal barrier shown by the downwards arrow in Fig.4.8. V_{TD}^L and V_{TD}^H are peak positions in Fig.4.9 for low and high V_0 respectively

	V_B	V_{TD}^L	V_{TD}^H	ΔV_B^L	ΔV_B^H
^{62}Ni	72.19	72	71	0.19	1.19
^{64}Ni	71.76	72	70	0.24	1.76
^{96}Zr	96.54	96	92	0.54	4.54
^{194}Pt	169.53	172	167	2.47	2.53
^{238}U	193.51	191	186	2.51	7.51

different peaks in Fig.4.9. These positions represent the barrier heights after the nominal barrier height has been split into different barriers, as a result of the coupling effect. In this table, V_B represents the nominal barrier height, that is obtained using equation (4.5)

$$V_B = V_N(R_B) + \frac{Z_P Z_T e^2}{R_B} \quad (4.5)$$

V_{TD}^L and V_{TD}^H correspond to positions of the peaks in Fig.4.8. In this table, we only consider the peaks which correspond to lower values than V_B . $\Delta V_B = V_B - V_{TD}^x$ ($x \equiv L, H$) represents the value reduced from the nominal Coulomb barrier height.

To conclude this section, we also analyse the effect of the multi-neutron transfer on the barrier distributions. We have seen in Fig.4.7 that multi-neutron transfer channels do suppress the fusion cross section above the Coulomb barrier, compared to the $+1n$ channel. The effect of multi-neutron transfer channels on the fusion barrier distributions is displayed in Fig.4.10, where we notice that neutron transfer channels produce different peaks in the fusion barrier distributions.

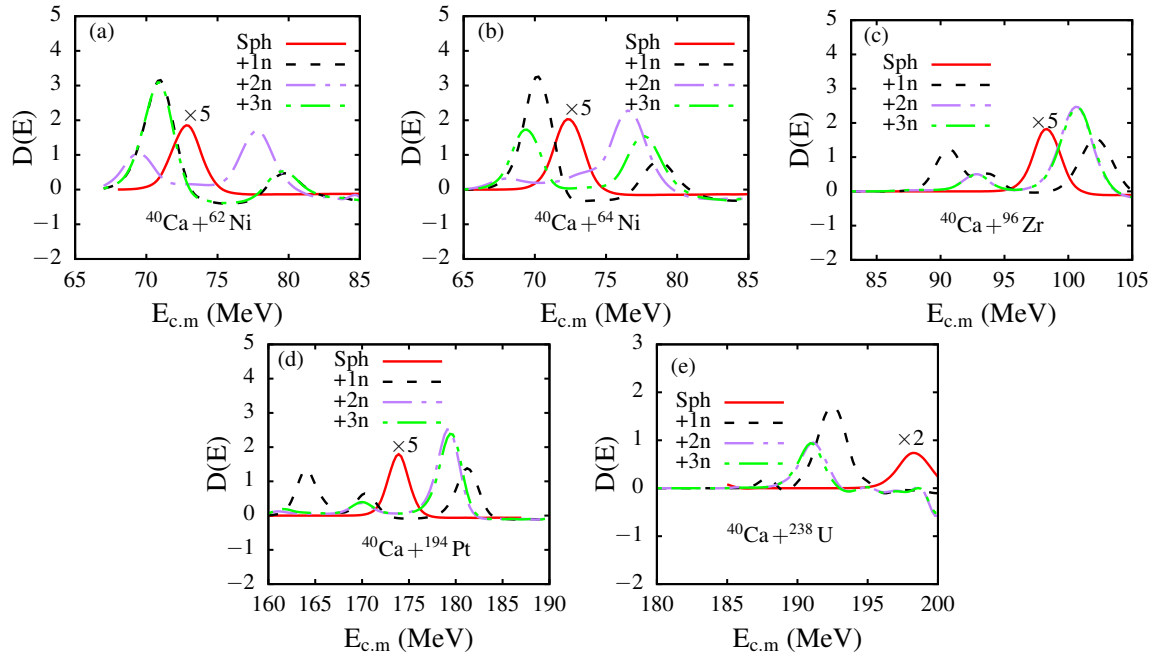


Figure 4.10: Effect of +1n,+2n and +3n transfer channel on fusion barrier distributions for ^{40}Ca -induced reactions. Label "Sph" represents the data for spherical collision where there is no target excitations.

Chapter 5

Conclusions

In this work we undertook a systematic study in understanding the rotational and vibrational effects on nuclear fusion reactions. To this end, we considered collisions of the following, (a) light projectile on light, medium and heavy targets (${}^6,{}^7\text{Li}$ induced reactions). (b) medium projectile on medium and heavy targets (${}^{40}\text{Ca}$ induced reactions). For a case of spherical collision, where there are no target internal excitations, fusion is mostly influenced by the height of the coulomb barrier and barrier penetration. The size of the potential well also influences fusion in spherical collisions. In our systematic approach, it was found that the potential well deepens with an increasing target mass, therefore a light-light collision reaction will have low fusion probabilities compared to light-heavy reaction. σ_F is also dependant on the radial positioning (r_{max}) of the colliding partners. When r_{max} is below the barrier position R_B , fusion is at it's lowest. σ_F is enhanced the most when $r_{max} \rightarrow R_B$. However, σ_F converges towards the same value when $r_{max} \gg R_B$. This theory has proven to be effective in all reactions under investigation from light to heavy collisions.

In the case of deformed target collisions, it was expected that the rotational quadrupole β_{20} and hexadecapole β_{40} deformation parameters should influence fusion. However, it is the sign of the deformation parameter that enhances or lower fusion. A positive parameter will enhance fusion even if the effects are small an negligible. By looking at total potential for heavy-heavy collision, we notice that every deformation parameter has an effect on the barrier height as well as the potential-well. It is well expected that a lowered Coulomb

barrier will enhance fusion given the incident energy is above barrier energy. However this is not the case when comparing Fig.4.4 to Fig.4.5. This is due to fusion enhanced by barrier penetrability at energies below and around the Coulomb barrier. This phenomena explains how increasing the potential depth V_0 enhances fusion at lower energies for both spherical and deformed collision reaction.

By analysing the fusion barrier distribution data, it was shown each positive parameter lowers the barrier and hence enhances fusion. The value of deformation parameters also plays a major role in a sense that when both parameters are included, the CCFULL code makes an average of the two deformation parameters and the output results will be similar to the results of the deformation parameter with a higher value. Therefore, rotational effects on fusion are dependent on the sign of the deformation parameter. When vibrational coupling is included, an increase in fusion enhancement was observed. However, it seems that σ_F is increased in comparison to rotational coupling when the collision partners are from a certain periodic group. Reaction including ^{96}Zr and ^{238}U yielded less σ_F for vibrational coupling compared to rotational coupling. This observation proves that the nuclear vibrations modify tunnelling probability and enhances below-barrier fusion excitation functions.

For the neutron transfer calculations, it is clear that for heavy collision systems the transfer channel is influenced by the Q-value of the system. For ^{40}Ca induced reactions we were able to deduce a trend that a lower Q-value enhances the most fusion regardless of the number of neutrons transferred during the reaction. However, this was not the case in $^{58,64}\text{Ni}$ reactions. The unusual trend found in Nickel reactions might be due to the similarity of the projectile-target nuclear masses and nuclear structures. In essence, none of the collision partners is overpowered by the other and as such the transfer channel does not only depend on the Q-value of the reaction but also on the target orientation θ . The authors of [44] concluded on the subject that transfer of few nucleons agrees with the experimental data whereas a large number of neutron transfer shows a shift towards neutron stripping which doesn't agree with the experimental data. As part of the recommendations, it was suggested that a systematic approach into the matter should

provide a more clear conclusion on how the nucleon transfer channel influences fusion. However in this research, such a systematic approach was considered and the results show that for +1n transfer, σ_F is induced the most in comparison with multi-neutron transfer channels.

Bibliography

- [1] O. N. Ghodsi and F. Lari, Phys. Rev. **C 89**, 054607 (2014)
- [2] P. Fröbrich and R. Lipperheide, *Theory of Nuclear reactions*, Oxford(1996)
- [3] P. Möller, A.J. Sierk, T. Ichikawa, H. Sagawa. Atomic data and nuclear data tables (2012)
- [4] T Rumin, K Hagino, and N Tagigawa, Phys. Rev. **C 61**, 014605 (1999)
- [5] L. F. Canto, P. R. S. Gomes, R. Donangelo, and M. S. Hussein, Phys. Rep. 424, 1 (2006).
- [6] N. Keeley, R. Raabe, N. Alamanos, and J. L. Sida, Prog, Part. Nucl. Phys. 59, 579 (2007)
- [7] S.A Alavi and V.Dehghani, Phys. Rev. **C 95**, 054602 (2017)
- [8] M. Ismail, W.M. Seif, H. El-Gebaly Physics Letters **B 563**, (2003)53-60
- [9] C. S. Palshetkar, S. Santra, A. Chatterjee, K. Ramachandran, S. Thakur, S. K. Pandit, K. Mahata, A. Shrivastava, V. V. Parkar, and V. Nanal, Phys. Rev. **C 82**, 044608 (2010).
- [10] V. V. Parkar, R. Palit, S. K. Sharma, B. S. Naidu, S. Santra, P. K. Joshi, P. K. Rath, K. Mahata, K. Ramachandran, T. Trivedi et al., Phys. Rev. **C 82**, 054601 (2010).
- [11] P. K. Rath, S. Santra, N. L. Singh, K. Mahata, R. Palit, B. K. Nayak, K. Ramachandran, V. V. Parkar, R. Tripathi, S. K. Pandit *et al.*, Nucl. Phys. A **874**, 14 (2012).

- [12] Denisov, V.Y., Pilipenko, N.A. *Interaction and fusion of deformed nuclei*. Phys. Atom. Nuclei **73**, 1152–1163 (2010)
- [13] M. Dasgupta, D.J. Hinde, N. Rowley, and A.M. Stefanini, Annu. Rev. Nucl. Part. Sci. **48**, 401 (1998)
- [14] V. Yu Denisov and S. Hofmann, Phys. Rev. **C 61**, 034606 (2000)
- [15] K. Hagino, N. Takigawa *Subbarrier Fusion Reactions and Many-Particle Quantum Tunnelling*, Progress of theoretical physics Vol. 128, No. 6 (2012)
- [16] K. Hagino and N. Rowley, Phys. Rev. **C 69**, 054610 (2004).
- [17] G. R. Satchler and W. G. Love, Phys. Rep. **55** (1979), 183.
- [18] B. Sikora, J. Bisplinghoff, W. Scobel et al., Physical Review, **C 20**, (1979) 2219
- [19] C. H. Dasso and A. Vitturi, Phys. Lett. **B 179**, 337 (1986).
- [20] D. Bourgin, S. Courtin, F. Haas et al., Physical Review, **C 90**, (2014) 044610
- [21] AM Stefanini, G. Montagnoli, H. Esbensen et al., Physics Letters, **B 728** (2014) 639-644
- [22] R. Vandenbosch, AA Sonzogni, JD Bierman, Journal of Physics, **G 23** (1997) 1303
- [23] J. Rangel, M.R Cortes, J. Lubian, L.F Canto *Quantum theory of complete and incomplete fusion in collision of weakly bound nuclei*. (2019), arXiv:1910.07925v1 [nucl-th]
- M. R. Cortes, J. Rangel, J. L. Ferreira, J. Lubian, and L. F. Canto Phys. Rev. **C 102**, 064628 (2020)
- [24] K. Nishio, S. Mitsuoka, I. Nishinaka et al., Physical Review, **C 86**, (2012) 34608
- [25] M. V. Andres, N. Rowley, and M. A. Nagarajan, Phys. Lett. **B 202**, 292 (1988).
- [26] G. Montagnoli and A. M. Stefanini, Eur. Phys. J. **A 53**, 169 (2017).
- [27] G. Montagnoli, A.M Stefanini, C.L Jiang et al., Physical review **C 85**, (2012) 024607

- [28] S. G. Steadman and M. J. Rhoades-Brown, *Annu. Rev. Nucl. Part. Sci.* **36**, 649 (1986).
- [29] B. B. Back, H. Esbensen, C. L. Jiang, and K. E. Rehm, *Rev. Mod. Phys.* **86**, 317 (2014).
- [30] PK Rath, S. Santra, NL Singh et al., *Physical Review*, **C 88**, (2013) 44617
- [31] PK Rath, S. Santra, NL Singh et al., *Nuclear Physics, A* **874** (2012) 14
- [32] PK Rath, S. Santra, NL Singh et al., *Physical Review*, **C 79** (2009) 51601
- [33] M. Dasgupta, DJ Hinde, K. Hagino et al., *Physical Review*, **C 66** (2002) 41602
- [34] A. Shrivastava, A. Navin, A. Diaz-Torres et al., *Physics Letters*, **B 718** (2013) 931
- [35] A. Di Pietro, P. Figuera, E. Strano et al., *Physical Review*, **C 87** (2013) 64614
- [36] Mandira Sinha, H. Majumdar, R. Bhattacharya et al., *Physical Review*, **C 76** (2007) 027603
- [37] M. Dasgupta, *et al.*, *Phys. Rev.* **C 70** (2004) 024606
- [38] P.R.S. Gomes, I. Patron, *et al.*, *Physical Review* **C 73**, 064606 (2006)
- [39] P.R.S. Gomes, R. Linares, *et al.*, *Physical Review* **C 84**, 014615(2011)
- [40] A. Shrivastava *et al.*, *Phys. Rev. Lett.* **103** (2009) 232702
- [41] Mandira Sinha *et al.*, *Eur. Phys. J* **A 44** (2010) 403
- [42] Manjeet Singh Gautam , Sukhvinder Duhan, Rishi Pal Chahal et al., *Physical Review*, **C 102** (2020) 014614
- [43] N.Rowley, G.R. Satchler, P.H. Stelson *Phys. Let.* **B 254** 25-29 (1991)
- [44] L.Corradi, J.H. He, D.Ackermann, *et.al.*, *Physical Review* **C 54**, 35020(1996)
- [45] K. Hagino, N. Rowley, A.T. Kruppa *Computer Physics Communications* **123** (1999) 143–152
- [46] AK Sinha, LT Baby, N. Badiger et al., *Journal of Physics*, **G 23** (1997) 1331

- [47] AM Stefanini, G. Fortuna, R. Pengo et al., Nuclear Physics, A 456 (1986) 509
- [48] M. Beckerman, M. Salomaa, A. Sperduto et al., Physical Review Letters, 45 (1980) 1472
- [49] M. Beckerman, M. Salomaa, A. Sperduto et al., Physical Review, C 25 (1982) 837
- [50] D. Ackermann, P. Bednarczyk, L. Corradi et al., Nuclear Physics, A 609 (1996) 91
- [51] A. Khan Int.J.Mod.Phys E Vol. 14, No. 2 (2005) 269–278
- [52] R. A. Broglia and A. Winther, *Heavy-Ion Reactions* (Addison-Wesley, New York, 1991).
- [53] R. Ogura, K. Hagino and C. A. Bertulani, Phys. Rev. **C 99**, 065808 (2019)
- [54] M. W. Kermode and N. Rowley, Phys. Rev. C 48 (1993), 2326.
- [55] M. Singh, Sukhvinder, R.Kharab, Nuclear Physics, A 897(2013) 179-197
- [56] Ian J.Thompson and Filomena M Nunes, *Nuclear reactions for astrophysics* (Cambridge, New York 2009)
- [57] L. Corradi, J. H. He, D. Ackermann, A. M. Stefanini, and A. Pisent Phys. Rev. C Vol 54,(1996)
- [58] G. R. Satchler, *Direct Nuclear Reactions*, Oxford 1983
- [59] M. Abramowitz and I.A. Stegun 1964, *Handbook of mathematical functions*, Washington(1964)
- [60] J. R. Leigh, M. Dasgupta, D. J. Hinde, J. C. Mein, C. R. Morton, R. C. Lemmon, J. P. Lestone, J. O. Newton, H. Timmers, J. X. Wei, and N. Rowley, Phys. Rev. **C 52**, 3151 (1995).
- [61] G. Kaur, B. R. Behera, A. Jhingan, B. K. Nayak, R. Dubey, P. Sharma, M. Thakur, R. Mahajan, N. Saneesh, T. Banerjee et al., Phys. Rev. **C 94**, 034613 (2016).

- [62] G. Montagnoli and A. M. Stefanini, Proceedings of the International Conference on FUSION11, Saint-Malo, France, 2–6 May 2011, EPJ Web of Conferences, edited by Ch. Schmitt, A. Navin, M. Rejmund, D. Lacroix, and H. Goutte (2011), Vol. 17, p. 05001.
- [63] G. Kaur, K. Hagino, N. Rawley, Physical Review **C 97**, 064606 (2018).
- [64] G. Kaur, B. R. Behera, A. Jhingan, B. K. Nayak, R. Dubey, P. Sharma, M. Thakur, R. Mahajan, N. Saneesh, T. Banerjee, Khushboo, A. Kumar, S. Mandal, A. Saxena, P. Sugathan, and N. Rowley, Phys. Rev. **C 94**, 034613 (2016).
- [65] V.I Zagrebaev and V.V Samarin, Physical Review **C 75**, 035809(2007)
- [66] V.I Zagrebaev and W Greiner, Physical Review **C 87**, 034608(2013)
- [67] V.I Zagrebaev Physical Review **C 67**, 061601(R) (2003)
- [68] V. I. Zagrebaev, Phys. Rev. **C 78**, 047602 (2008).
- [69] V.A Rachkov, A. Karpov *et al.*, Physical Review **C 90**, 014614 (2014)
- [70] H.Q Zhang, C.J.Lin, H.M.Jia, X.X. Xu, et al., Physical Review **C 82**, 054609 (2010).
- [71] A.V.Karpov, V.A.Rachkov, V.V.Samarin, Physical Review **C 92**, 064603 (2015)
- [72] M.M. Shaikh, S.Roy, A. Mukherjee *et.al*, Phys Rev **C 102**, 024627 (2020)
- [73] A. B. Balantekin and P. E. Reimer, Phys. Rev. **C 33**, 379 (1986).
- [74] H. Timmers, J. R. Leigh, M. Dasgupta, D. J. Hinde, R. C. Lemmon, J. C. Mein, C. R. Morton, J. O. Newton, and N. Rowley, Nucl. Phys. A 584, 190 (1995).
- [75] J.J.Kolata, A. Roberts, A.M Howards, Physical Review **C 85**, 054603 (2012)
- [76] Takatosho Ichikawa, Physical Review **C 92**, 064604(2015)
- [77] H. Timmers, *et al.*, Nucl. Phys. **A 633**, 421 (1998).
- [78] H. Zhang, F. Yang, C. Lin, Z. Liu, and Y. Hu, Phys. Rev. **C 57**, 1047(R) (1998)

- [79] R. F. Simões, D. S. Monteiro, L. K. Ono, A. M. Jacob, J. M. B. Shorto, N. Added, and E. Crema, *Phys. Lett.* **B 527**, 187 (2002).
- [80] E. Piasecki, Ł. Świdorski, N. Keeley, M. Kisielinski, M. Kowalczyk, S. Khlebnikov, T. Krogulski, K. Piasecki, G. Tiourin, M. Sillanpaa, W. H. Trzaska, and A. Trzcinska, *Phys. Rev.* **C 85**, 054608 (2012).